ACTIVE CONTROL OF HIGH SPEED JETS FOR NOISE MITIGATION

A Thesis

Presented in Partial Fulfillment of the Requirements for

Graduation with Distinction in the

Department of Mechanical Engineering at The Ohio State University

By

Amy Eileen McCluskey

****

The Ohio State University

May 2007

Examination Committee:

Dr. M. Samimy, Advisor

Dr. I. Adamovich

Approved by

_____

Advisor
Department of Mechanical Engineering

- **Abstract**

Research, design, and experimentation were performed in the Gas Dynamics and Turbulence Laboratory at The Ohio State University to control far-field noise for high-speed jets and observe the effects of control with the purpose of noise mitigation. Recently localized arc filament plasma actuators (LAFPA) were developed to force an axisymmetric Mach 0.9 jet. Previous experimentation was improved upon by adding four actuators to an eight actuator equally spaced setup. A new nozzle extension was designed to house these twelve actuators and an adaptor was developed to provide flush mounting of the electrodes of the actuators between the nozzle and extension. The twelve actuators were used to excite the flow over a large frequency range, which was expressed in terms of the non-dimension forcing Strouhal number (St_{DF}). Microphones, mounted at angles of 30° and 90°, were used to collect far-field sound pressure levels.

The response of the jet varied greatly with azimuthal mode and St_{DF}. The perturbations were observed to greatly affect the far-field sound pressure levels at St_{DF}'s between 0.1 and 5. Furthermore, greater noise mitigation was recorded at higher modes such as azimuthal modes 5 and ±6. This was contrasted to the enhanced mixing observed at lower modes such as m = 1 or ±1. However, the effects of actuation on the flow were independent of azimuthal mode when forced at a St_D higher than about 2. While these patterns and results were observed at an angle of 30° to the jet axis, the effects remained unclear at an angle of 90°. However, the general observation was made that forcing at higher modes significantly reduces far-field noise.

ACKNOWLEGDEMENTS

I would like to thank Professor Samimy for all of his wisdom and guidance. He helped with my decision to pursue undergraduate research and then assisted me throughout the entire project. He provided the motivation, definition, and resources for the entire project. Additionally, I would like to thank Jeff Kastner and Jin-Hwa Kim for their knowledge and assistance with experimentation and design. Furthermore, I would like to thank everyone at the GDTL for their assistance and resources.

- **Table of Contents**

List of Figures

CHAPTER

1.0 INTRODUCTION

With a surge of interest in creating undetectable, stealth aircrafts, high far-field noise levels continues to be a problem. During takeoff and landing, the noise level of an aircraft can approach approximately 110 dB. At typical cruising altitudes, the amplitude of the noise level may drop to approximately 40 dB. While the decrease in noise levels during flight is substantial, the noise levels remain loud enough to be detected. In addition to the application in stealth aircrafts, noise mitigation can also be helpful to commercial aircrafts. A reduction in noise would provide greater flexibility in flight path and time because community noise restrictions would no longer limit the flight pattern choices. While many aspects of the aircraft can contribute to this noise, the main source of far-field noise during take-off is flow through the exhaust of the aircraft [2].

In addition to the sound pollution, noise produced during flight can also cause structural damage to the shell of the plane. This structural damage is more often a result of flow over a shallow cavity experienced during the deployment of weapons or

landing gear. Figure 1.1 shows flow over a shallow cavity which results in resonance and eventually structural damage.

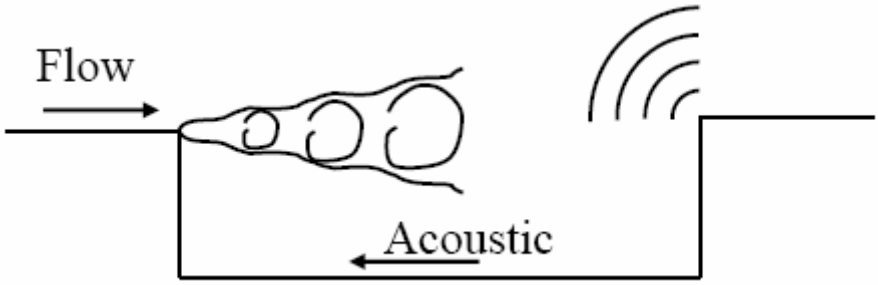

Figure 1.1: Sound Perturbation Produced Due to Flow over a Cavity [1]

In contrast to flow over a cavity which can lead to extensive structural damage, flow through the exhaust of an aircraft results in far-field noise. While localized noise resulting in structural damage is also present, it is much less significant than the far-field noise. Figure 1.2 below shows how flow structures develop in the axisymmetric jet which lead to far-field noise.

Figure 1.2: Flow Structures in an Axisymmetric Jet

This effect strongly counteracts efforts to improve the stealth of aircrafts. On a commercial level, a more quiet aircraft would not be restricted by community noise pollution laws and, therefore, could fly more direct routes saving time and fuel.

Control and mitigation of this localized and far-field noise was proposed to result in longer life of aircraft parts, smoother operation, and greater flexibility in

flight path. Various methods have been explored in order to control noise as documented in previous research. Details of this experimentation will be included in the background in Chapter 2. Based on this previous research, a method was chosen and experimentation was conducted in the GDTL to investigate the effectiveness of plasma actuators with respect to noise mitigation [4].

A Mach 0.9 nozzle with an exit diameter of 1 in was used to model the jet exhaust. The room temperature air was dried and compressed to 16 MPa in tanks with a capacity of 16 in^3. Localized Arc Filament Plasma Actuators (LAFPA) were utilized to excite various azimuthal modes in the flow. These modes were forced at Strouhal numbers varying from approximately 0.1 to 5. The details of the problem definition, design of components, experimental facility, and experimental results were included in the present work. Further testing will be conducted to obtain flow visualization and explore the use of plasma actuators to control heated jets.

CHAPTER

2.0 BACKGROUND

As previously mentioned, flow over and through an aircraft exhaust has been observed to instigate both localized and far-field noise, each with its own implications on flight. Structural damage is inflicted on an aircraft by localized noise. Cracking and fatigue have been observed in the outer shells of aircrafts. In addition, aircrafts are limited to certain flight patterns due to the far-field noise restrictions in many residential areas [3].

Due to these problems associated with jet noise, research was conducted with the purpose of arriving at a solution and means of controlling the jet noise. A thorough literature review was conducted to understand the source of the noise as well as understand previous attempts to reduce noise using energy-efficient means. Finally, initial solutions were posed and experimentation was performed. Discussions of this background information, previous research, and initial solutions are included in the following sections.

2.1. Free Shear Layer Instability

The planar free shear layer in a flow acts as an amplifier for natural disturbances present in the flow. This instability is referred to as the Kelvin-Helmholtz instability, also known as the inviscid instability in high Reynols numbers where the effect of viscosity is relatively low. Through observation of previous research, the dynamics of these natural and random instabilities are generally accepted to be responsible for bulk mixing in fluids and the source of far-field radiated noise. The random nature of these disturbances cause jitter in the vortex roll up, which results in large-scale structures that are not spatially coherent. Consequently, there is a need to manipulate and control these disturbances. Low amplitude forcing in the shear layer has resulted in a dramatic effect on the flow, allowing for organization in the flow structures and merging processes [3].

2.2. Axisymmetric Jets

Axisymmetric jets add complexity to the effects of the planar shear layer in multiple ways. Azimuthal modes in the axisymmetric jets compete for energy and grow selectively. In addition, the growth of the free shear layer inward toward the centerline axis results in the decay of the jet centerline velocity and the ending of the jet potential core. Furthermore, as the growth increases, the nature of the interaction of the flow structures changes from typical merging of successive large-scale structures to azimuthal interaction. Due to this phenomenon, linear stability analysis is not applicable for understanding the free shear layer and the early development of

the shear layer roll up. This requires that new innovative methods be used in understanding and controlling the merging [3].

2.3. Flow Control

Flow control is used to modify the flow characteristics and can be divided into two top level categories. Passive control involves physical geometric modifications to the system while active control involves the addition of mass or energy into the flow. Both approaches are used to manipulate various instabilities within the flow. Active control is then further divided into open-loop and closed-loop control. In closed-loop control, the flow model and information from a sensor in the flow guides the actuation process. With open-loop control, actuations are determined by either the operator's command or predetermined [2].

In recent years, passive control has been used extensively for mixing modifications and noise mitigation. With passive control, streamwise vorticity is generated by geometric modifications made to the nozzle or splitter plate trailing edge [4]. Such geometric modifications include tabs or chevrons. These modifications can successfully reduce noise. However, these permanent modifications do not allow the user any flexibility in operation, and can have an adverse effect on the plane during flight [3]. For example, added tabs and chevrons may increase drag during takeoff or landing. Figure 2.1 shows the use of chevrons to reduce noise on an aircraft.

Figure 2.1: Aircraft Exhaust with Integrated Chevrons (courtesy of www.nasa.com)

In contrast to passive control, active control provides the user with more flexibility, as the application can be turned on and off as needed. Open-loop active control is classified into two categories: steady or low frequency mass or energy addition and higher frequency addition, which is in the range of flow instabilities. Steady or low frequency mass or energy addition includes fluidic injection through micro-jets and fluidic chevrons. While these fluidic chevrons are considered active control due to the addition of energy to the system, these methods do not harbor frequency or phase control, which is essential for exciting flow instabilities. High frequency actuation allows for manipulation of instabilities in the shear layer and is a part of the research topic and experimentation discussed throughout the present work [2].

Extensive work involving control of low-speed, low Reynolds number flows has previously been conducted. However, complications arise with an increase in Reynolds number as the background noise, instability frequencies, and flow momentum increase accordingly. To counteract this effect, actuations must occur at

higher amplitude and higher frequency, which are two diametrically opposing parameters. For the research described in the present work, both high-speed and high Reynolds number flows were considered. In addition, due to this level of difficulty in actuation, very few methods for this actuation have been developed and will be discussed in the following sections.

2.3.1. Acoustic Excitation

Acoustic drivers have revealed various flow instability characteristics and correlations to far-field sound levels. Forcing the flow around the jet column instability led to the amplification of the broadband noise, the presence of a high amplitude tone at the forcing frequency in the far-field, and an increase of turbulence intensity in the flow field. When the jet was forced with various azimuthal modes of the jet column instability, broadband noise increased but the amplitude of the radiated tones appeared to be weakened. The investigation of the acoustic field for jets excited at frequencies higher than the jet column instability revealed a minor reduction in broadband noise. However, the acoustic forcing proved to be limited by the actuator as both high amplitude and high frequency actuations could not be attained [2].

2.3.2. Thermal Actuation

The high amplitude and high frequency actuations that are required to perturb high-speed jets can be achieved through the use of electric discharge plasma. As a

result, there has been a recent surge in the investigation, the development, and the use of plasma actuators.

Electrohydrodymanic (EHD) and Magnetohydrodymanic (MHD) are two primary mechanisms of plasma flow control. Both involve motion through collision momentum transfer from charged species accelerated in the plasma by Coulomb and Lorentz forces, respectively. Joule heating that exists in the electric discharge plasma or in the plasma generated by the laser breakdown heats the flow. However, both of these mechanisms are limited. With EHD flow control, significant ion density in the space region of the electric discharge must be generated. While energy efficient, EHD flows appear impractical for use in high-speed jets. In addition, MDH flow control requires that significant flow conductivity is maintained. This method requires a high plasma power budget and is not very efficient [3].

In addition to MHD and EHD, purely thermal flow control includes bulk heating of the flow by diffuse nonequilibrium plasma, localized heating by plasma torch, or pulsed laser breakdown. While these methods have been used at relatively low static pressures, both require a very large power supply and are, therefore, inefficient. In contrast to these methods, plasmas in high current electric discharges result in intense, localized, rapid heating. It is well-known that this heating may produce shock waves and significantly alter the flow over blunt bodies. The heating causes abrupt changes in the pressure of the flow and suggests that rapid heating near the surface of high speed flows can be used to excite flow instabilities.

2.3.3. Plasma Actuation

In contrast to EHD, useful only in low-speed flows, and MHD, only practical in low-pressure flows, current experimentation has shown that the localized arc plasma method is the only energy efficient way to excite flow instabilities in high-speed jets and high Reynolds number jets over a large range of static pressures. This method utilized rapid, localized, near-adiabatic heating that occurs near the surface of the jet, alters the flow pressure, and affects the flow instabilities. Besides the favorable energy efficiency of plasma actuation, this method triumphs over acoustic and mechanical actuation as it allows for a unique combination of various forcing frequencies and amplitudes to be used. In addition, multiple actuators can be operated at once and the user has greater control over input parameters such as repetition rate, duty cycle, and phase. Due to these parameters and flexibility in operation, specific instabilities, such as the jet column instability and shear layer instability, can be excited along with their respective azimuthal modes. Significant flow field changes can be made at a relatively low energy costs [3].

2.4. Azimuthal Mode Definition

With axisymmetric jets, an increase in growth leads to azimuthal interaction in the flow. Therefore, forcing at azimuthal modes is used in order to control the natural instabilities in the shear layer. The modes are defined through actuator phase changes and time delays. First, a spatial phase is assigned to each actuator in the set. These phases are determined by:

$$\phi_a = \frac{2\pi}{n}(a-1) \tag{1}$$

where a is the actuator number, n is the total number of actuators, and ϕ_a is the azimuthal location associated with the particular actuators in radians. Next, the time delay is calculated for each spatial phase by:

$$\tau_a = m\phi_a / 2\pi f_F \tag{2}$$

where ϕ_a is the azimuthal location in radians, f_F is the forcing frequency in Hz, m is the azimuthal mode number (i.e. 1, 2, 3), and τ_a is the time delay for the particular actuator in seconds. In addition the pulse width or on-time, which is equal for all actuators, is calculated by:

$$p_{width} = \delta / f_F \tag{3}$$

where f_F is the forcing frequency in Hz, δ is the duty cycle expressed as a fraction, and p_{width} is the pulse width for each actuators in seconds.

All of the equations are then transformed to the time domain and combined into one function. This general function, *g(t)*, is used to determine the input signal for the particular actuator. The following shows this combination with normalized amplitude of 1 V:

$$g(t) = \begin{cases} 0 & if \quad 0 < t < m\phi_a / 2\pi f_F \\ 1 & if \quad m\phi_a / 2\pi f_F < t < \delta / f_F + m\phi_a / 2\pi f_F \\ 0 & if \quad \delta / f_F + m\phi_a / 2\pi f_F < t < 1 / f_F \end{cases} \tag{4}$$

where f_F is the forcing frequency in Hz, δ is the duty cycle expressed as a fraction, p_{width} is the pulse width for each actuators in seconds, ϕ_a is the spatial phase in radians, m is the azimuthal mode number (i.e. 1, 2, 3), and τ_a is the time delay for the particular actuator in seconds [4].

CHAPTER

3.0 PREVIOUS WORK WITH 8 ACTUATORS

Previous experimentation in the Gas Dynamics and Turbulence Laboratory at The Ohio State University was conducted on high-speed jets using plasma actuators. A nozzle extension made from boron nitride was designed to house all of the actuators and attach to the exit of the nozzle. Eight plasma actuators were mounted with equal spacing to the extension and were used to perturb the flow. This arrangement allowed for the flow to be excited with simple azimuthal modes 0, 1, 2, and 3 and mixed modes ±1, ±2, ±3, and ±4.

With this 8 actuator setup, flow visualization data sets were recorded to visually document the effect of the actuation on the flow patterns. As seen in Figure 3.1, the flow structures were not visible with the baseline case. Each tick mark in

represented a distance of x/D=1 away from the nozzle exit where x is the distance and D is the diameter.

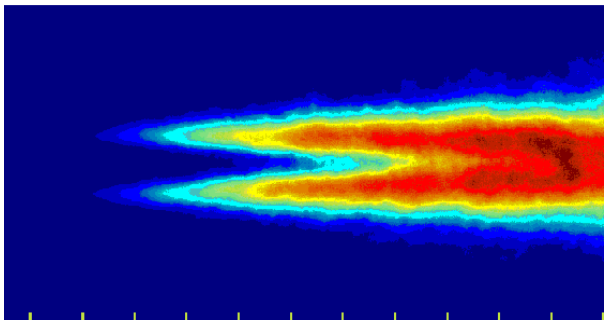

Figure 3.1: Ensemble-averaged Stream-wise Images for Baseline Jet

In contrast to the baseline case, flow structures developed when the high-speed jet was forced with various azimuthal modes. Figure 3.2 shows the flow visualization results from azimuthal modes 0, 1, and ±1. Forcing with m = 0, the axisymmetric mode, resulted in flow structures that were in phase and symmetric. However, forcing mode 1, the first helical mode, showed flow structures that were out of phase. The same out of phase structures can be seen for forcing with mode ±1.

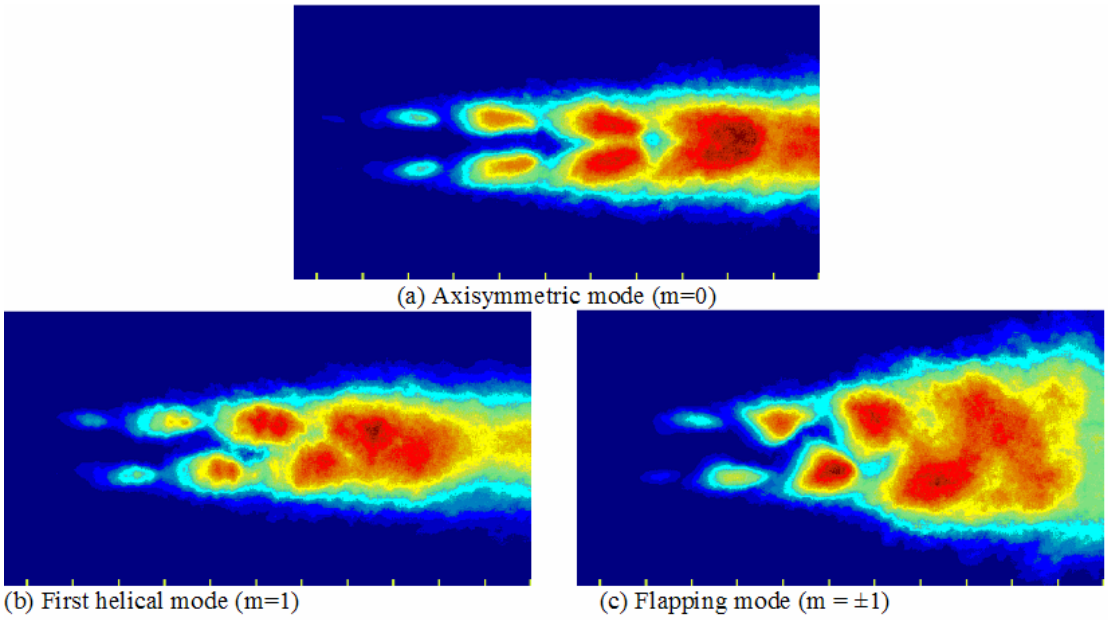

Figure 3.2: Ensemble-Averaged Streamwise Images for Modes 0, 1, and ±1

In addition to the flow visualization data sets, two ¼“ B&K microphones were mounted at 30° and 90° to capture the far field sound pressure level (SPL). Overall sound pressure levels were calculated and compared to the baseline jet to evaluate noise mitigation. The overall sound pressure level, or OASPL, at various forcing Strouhal numbers (St_{DF}'s) was plotted for modes 0, 1, 2, and 3 and can be seen in Figure 3.3. The forcing effect was very different at 30° and 90° angles. Greater noise mitigation was observed at 30° than at 90°. When forced at a Strouhal number (St_D) greater than 2, no differences were observed between modes. This signified that forcing at very high frequencies did not have much affect on the flow. Additionally, greater noise mitigation was observed in greater azimuthal modes, especially at mode 3. As shown in Figure 3.3(a), the change in OASPL when forced at mode 3 dipped farther below zero than other modes at a St_D of approximately 1.3.

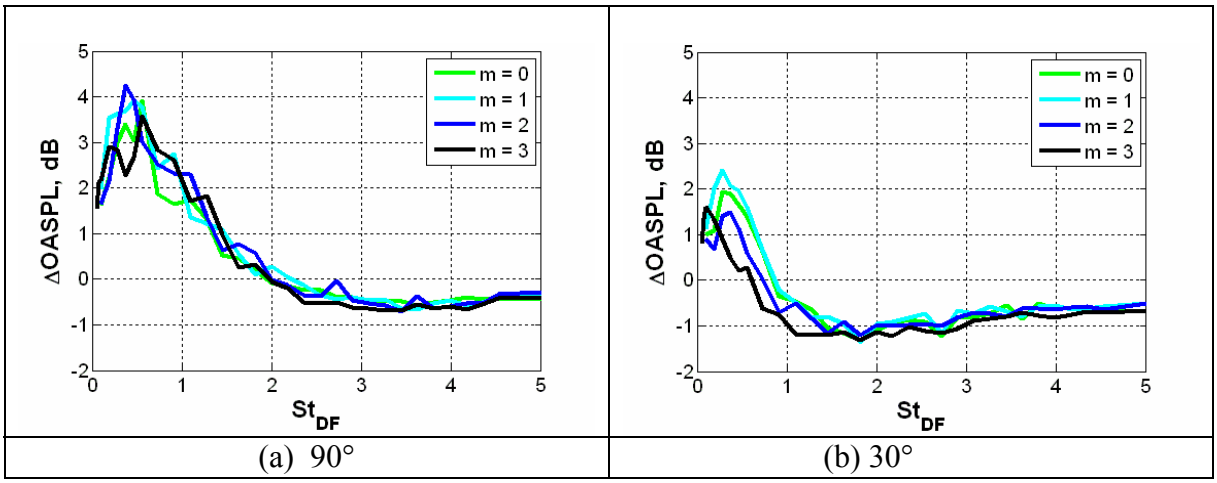

Figure 3.3: Change in OASPL for Azimuthal Modes Using 8 Actuators at (a) 30° and (b) 90°

In addition to simple azimuthal modes, the axisymmetric jet was excited with mixed modes ±1, ±2, ±3, and ±4. These results were included in Figure 3.4. These results indicated that the OASPL was increased more with the first two mixed modes (m = ±1 & ±2), especially at 30°. The peak ΔOASPL increased from 2.4 dB to 4.3 dB at 30°. While the mixed modes increased the jet noise, the same trend was observed. High mixed modes led to a lower OASPL.

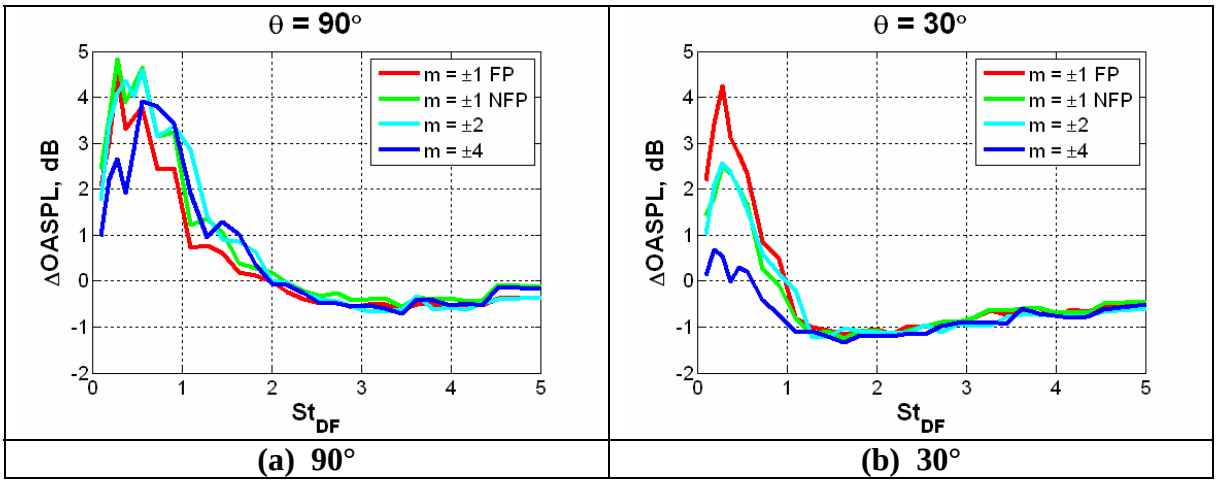

Figure 3.4: Change in OASPL for Mixed Modes Using 8 Actuators at (a) 30° and (b) 90°

Since greater noise mitigation was observed at higher azimuthal modes, it was desired to test at higher modes. However, a spatial Nyquist criteria required that two times the number of actuators be greater than the azimuthal mode number. Therefore, the highest mode attainable with eight actuators was 3 and ±4. As a result, my research focused on implementation of 12 actuators and running experiments up to mode 5 and ±6.

CHAPTER

4.0 EXPERIMENTAL METHODOLOGY

4.1. Design of Components

In order to achieve the higher modes as previously discussed, various aspects of the design were altered and changed. A new nozzle extension was designed to house all 12 actuators. In addition, an adaptor was created to fit the extension to the nozzle. Furthermore, the wiring design and setup from experimentation of eight actuators, was adapted to fit the new setup with 12 actuators. The details of the design are included in the following sections.

4.1.1. Nozzle and Adaptor Design

The previous design of the extension with eight actuators can be seen in Figure 4.1. The extension was made from boron nitride. The innermost hole on the extension was designed to fit to the nozzle exit and be flush against the inner wall of

the nozzle. In addition, the medium size holes were created to attach the extension to the nozzle. Finally, the small size holes were designed to hold the actuators in place.

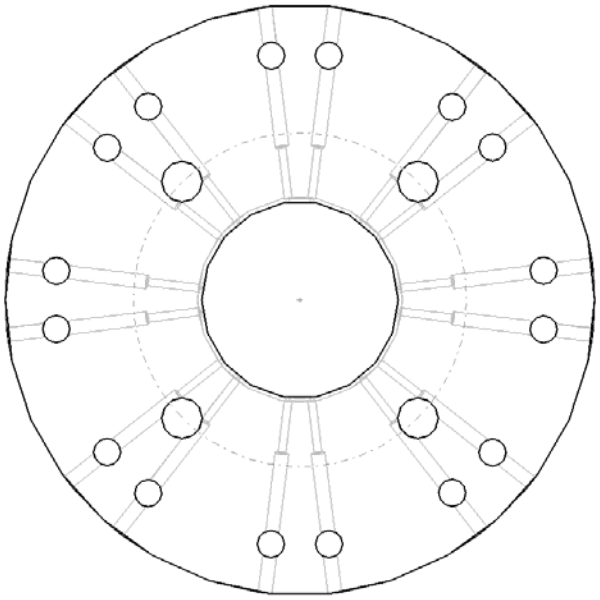

Figure 4.1: Previous Nozzle Extension Design for 8 Actuators

While this design was sufficient for eight actuators, modifications were required to fit the new intentions of the experimentation. To achieve proper operation and arcing, the spacing between the actuators had to be greater than the spacing between the electrodes. To achieve this, the holes used to screw the extension to the nozzle were moved outward from the inner diameter, closer to the edge of the extension. This led to a misalignment problem with mounting the extension to the nozzle. Due to this problem, an adaptor was also designed with its main purpose being to fit the nozzle to the extension and keep the inner surfaces flush.

The final design for the nozzle extension was included in Figure 4.2. A picture of the fabricated part was included in Figure 4.3. The diameter of the opening for the extension was 1 in. This matched the inner exit diameter at the nozzle exit and

consequently the adaptor. The outer diameter of the nozzle extension was 3 inches to ensure that the actuators could be mounted and secured. The spacing between the electrodes was designed to be 3 mm, with a spacing of approximately 4 mm between the actuators. This provided a difference in spacing so that the plasma would arc between the positive and negative electrodes of a particular actuator. The extension was made from boron nitride. This material proved to be strong enough to hold the components, mount to the nozzle, and handle the plasma arcing.

To meet the need of attaching the extension to the nozzle, an adaptor was designed. As seen in Figure 4.4, the adaptor was approximately the same size as the extension. The inner diameter was 1 in, just like the extension. The four outer holes functioned as screw holes for mounting to the extension. The five outer holes were used to mount the adaptor to the nozzle. The total adaptor, extension, and nozzle assembly can be seen in Figure 4.4. All three components fit together and the inner diameters ensured a flush fit. The model of the assembly was included and can be seen in Figure 4.5.

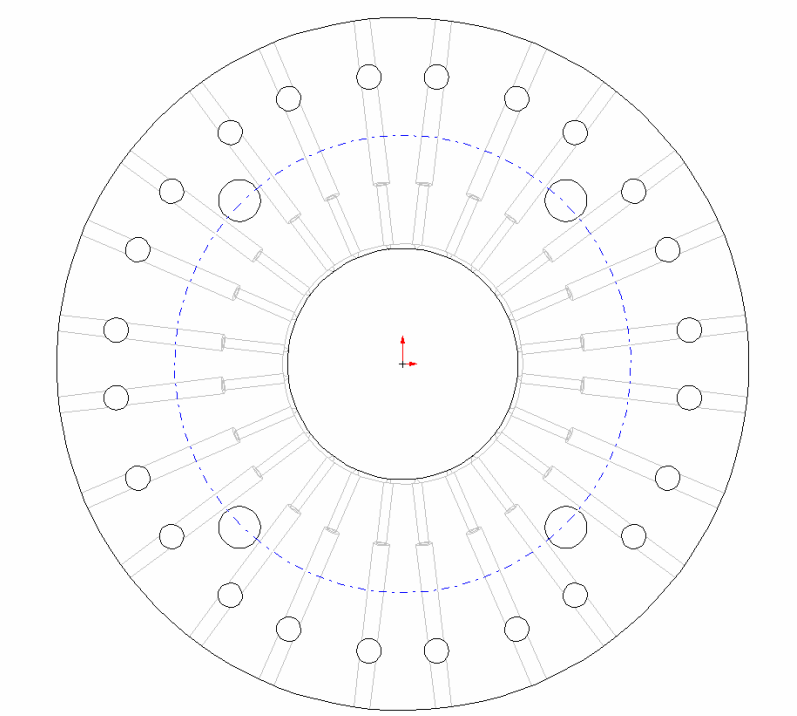

Figure 4.2: Final Design for 12 Actuator Extension

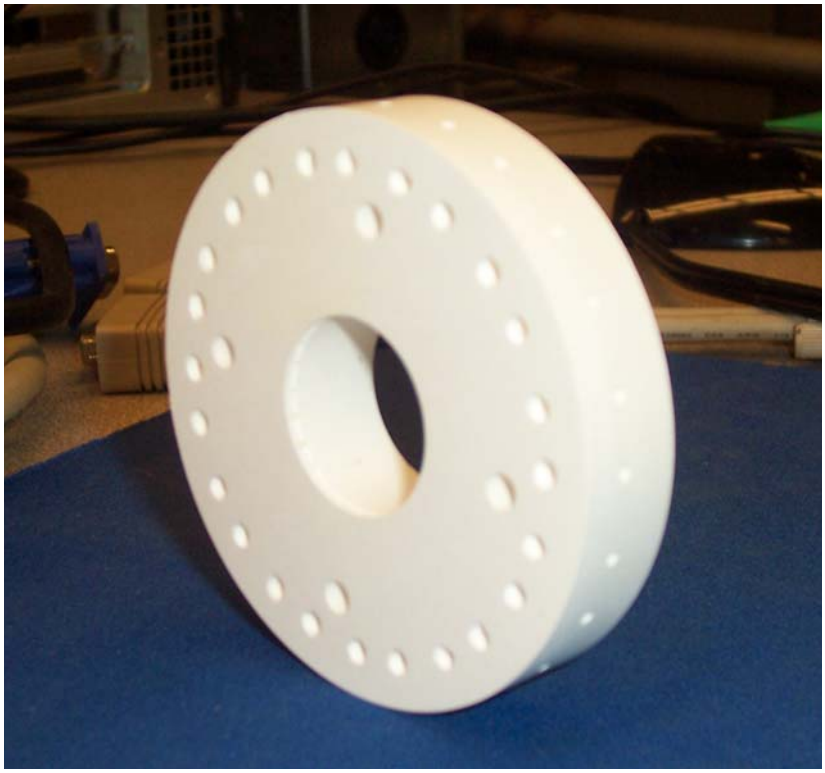

Figure 4.3: Picture of the 12 Actuator Nozzle Extension

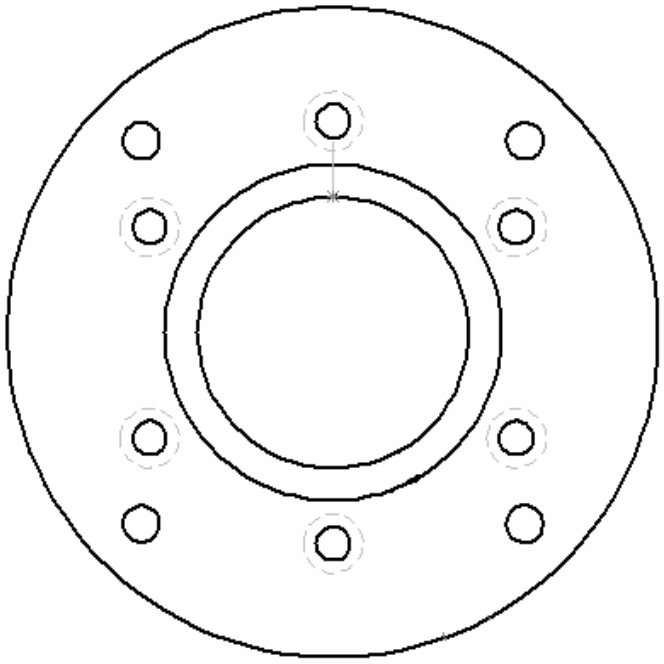

Figure 4.4: Final Adaptor Design

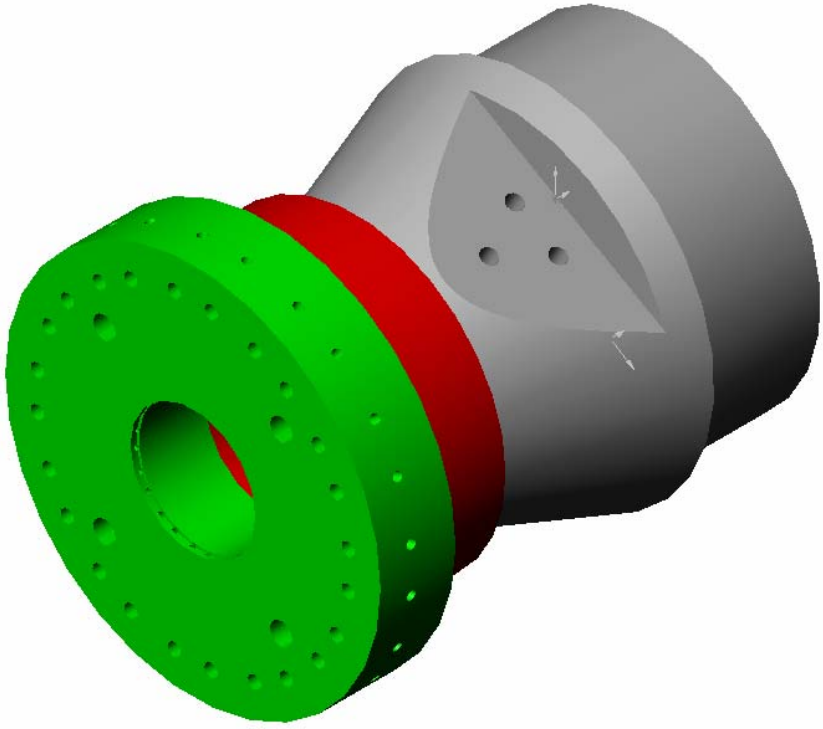

Figure 4.5: Assembly of Extension (green), Adaptor (red), and Nozzle (grey)

4.1.2. Wiring Design

To operate the plasma actuators, a plasma generator was created in house. The purpose of the generator was to send a high voltage signal to the pin electrodes of a particular actuator. This was achieved through the use of various electrical components and two DC power supplies. Figure 4.6 demonstrates the plasma generator wiring design for use with 8 actuators. Two power supplies were utilized for all 8 actuators. This power was then sent to eight different channels. Each channel consisted of a transistor switch, sandwiched between two high power resistors and followed by the pin electrodes associated with the particular actuator.

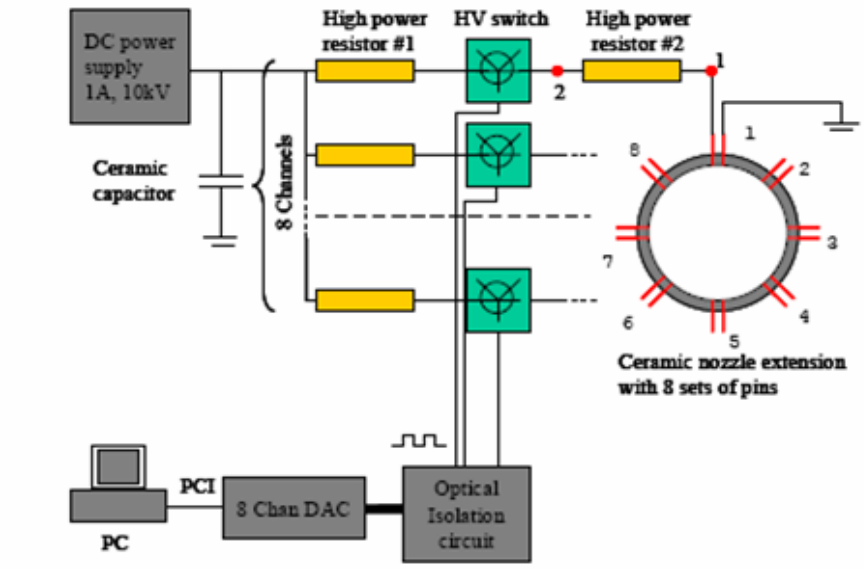

Figure 4.6: Previous Plasma Generator Wiring Diagram for 8 Actuators

A very similar design was developed for the twelve actuator setup. Figure 4.7 shows the electrical diagram for 12 actuators. Four channels were added to the previous design, including a total of 8 high power resistors and 4 transistors.

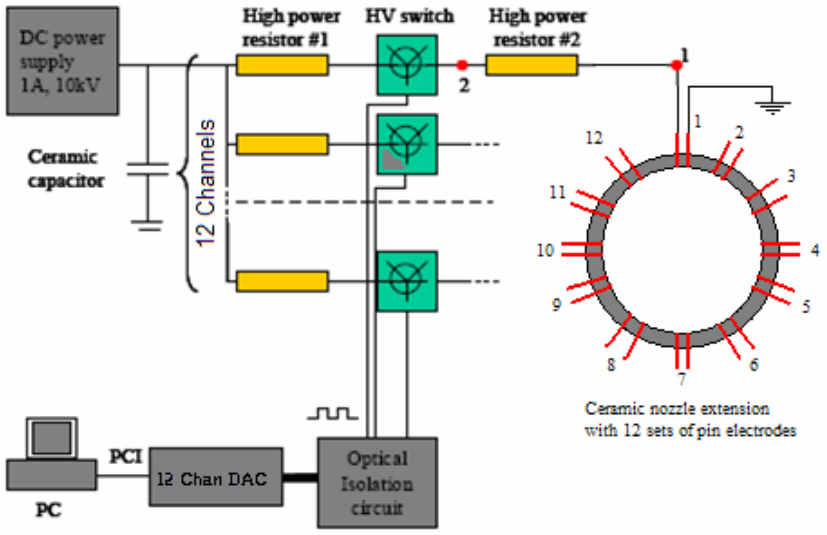

Figure 4.7: Plasma Generator Wiring Diagram for 12 Actuators

The high power resistors used in the electrical setup were ceramic and rated for 15 kΩ. Furthermore, a Behlke 10 kV, 30 Amp transistor switch was chosen as it allowed for fast response time and could handle the high voltage signal. Each DC power supply (Glassman High Voltage, Inc.), capable of supplying 10 kV and 1 A, was responsible for powering six actuators. Therefore, with all actuators firing at the same time, the current for each actuator was limited to approximately 0.17 A. Figure 4.8 shows one of the power supplies used for experimentation. Furthermore, the cart used to house the power supplies, resistors and transistors was included in Figure 4.9. A detailed picture of the transistor switches was included in Figure 4.10. These transistors were located on the cart. As with the 8 actuator setup, a house-built optical isolation circuit was implemented in the low voltage side.

Figure 4.8: Power Supply Used for Experimentation

Figure 4.9: Resistor and Transistor Cart Used for Experimentation

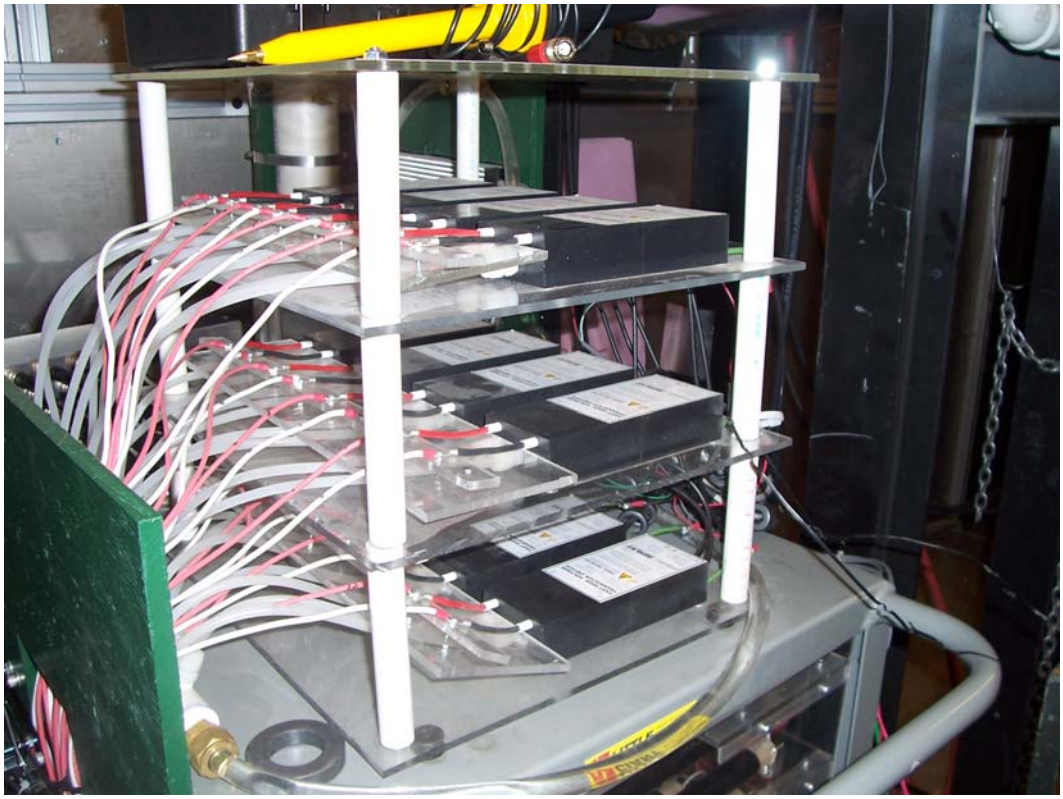

Figure 4.10: Transistor Switches Used for Experimentation

During experimentation, the high voltage signal sent through the electrical wiring and was ultimately sent to the positive pin electrode of the actuator. This allowed for plasma to arc between this positive electrode and the ground electrode. The data to analog converter that was included in Figure 3.10 will be discussed further in Section 6.0.

4.2. Azimuthal Mode Definition for 12 Actuators

Experimentation with 12 actuators was performed based on the definition presented in Section 2.0. The equations from that section were utilized to calculate

the input *g(t)* function, simulate the input signal, and simulate the actuator response. Details for all modes used in experimentation have been included in the following sections.

4.2.1. Input Pulse Generation

For all actuators and all azimuthal modes, the input function, *g(t)*, is comprised of a series of pulses that resemble rectangular waves. These input pulses determine the behavior of all actuators. When the actuators are sent a positive voltage, the switch opens and an arc is developed. In contrast when a zero voltage input signal is sent, the switch closes and the actuator is turned off. Figure 4.11 shows a simulated input signal, *g(t)*, for azimuthal mode 0 with a frequency of 10 kHz and a duty cycle of 10%. Azimuthal mode 0 is a simple mode to define and excite as all actuators are in phase.

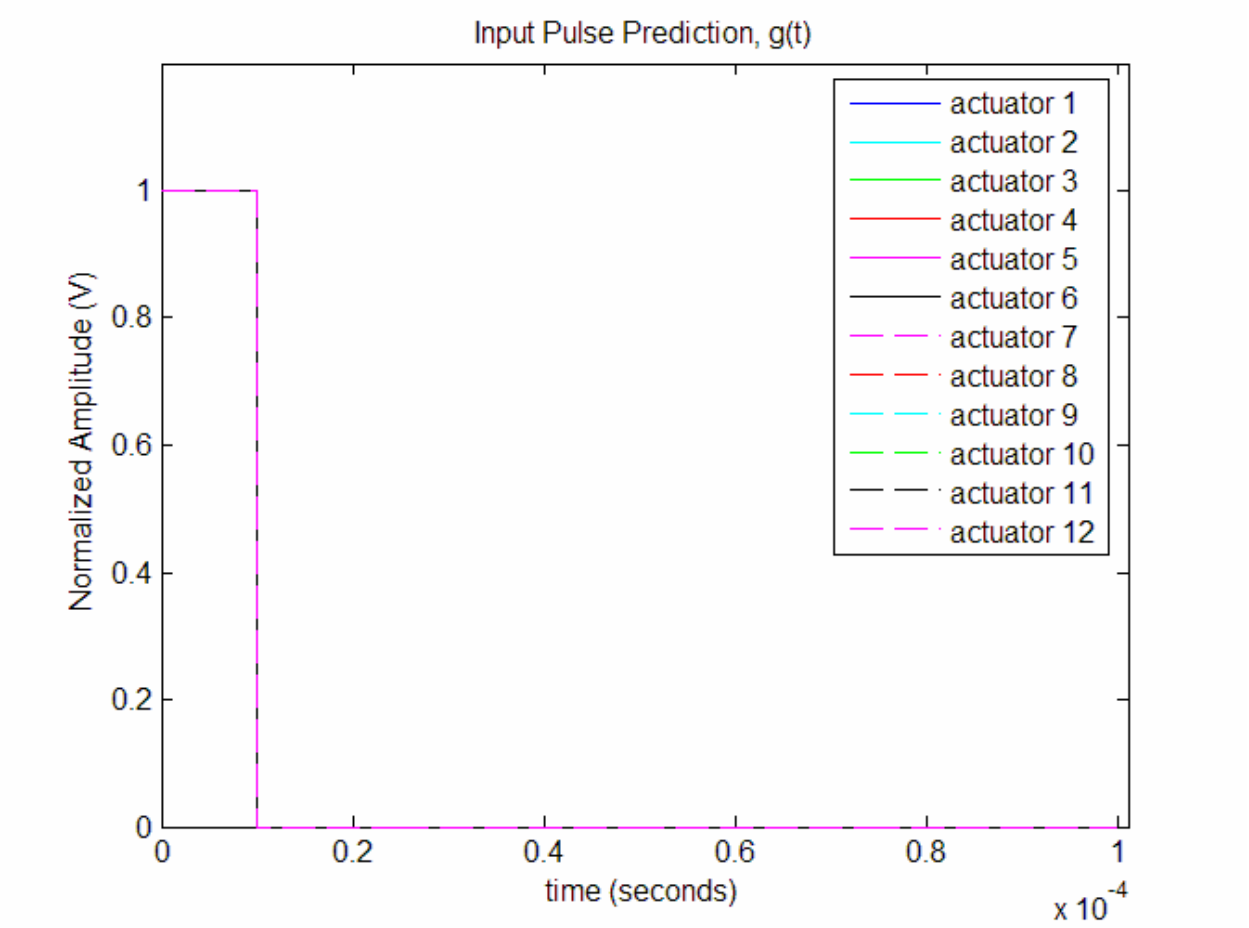

Figure 4.11: Input Pulse Simulation of Azimuthal Mode 0 for 10 kHz, 10% Duty Cycle

As the azimuthal mode changes, the forcing becomes more complicated. Figure 4.12 shows a simulated input signal, *g(t)*, of azimuthal mode 1 for all 12 actuators. For this simulation, an excitation frequency of 10 kHz and duty cycle of 5% were simulated.

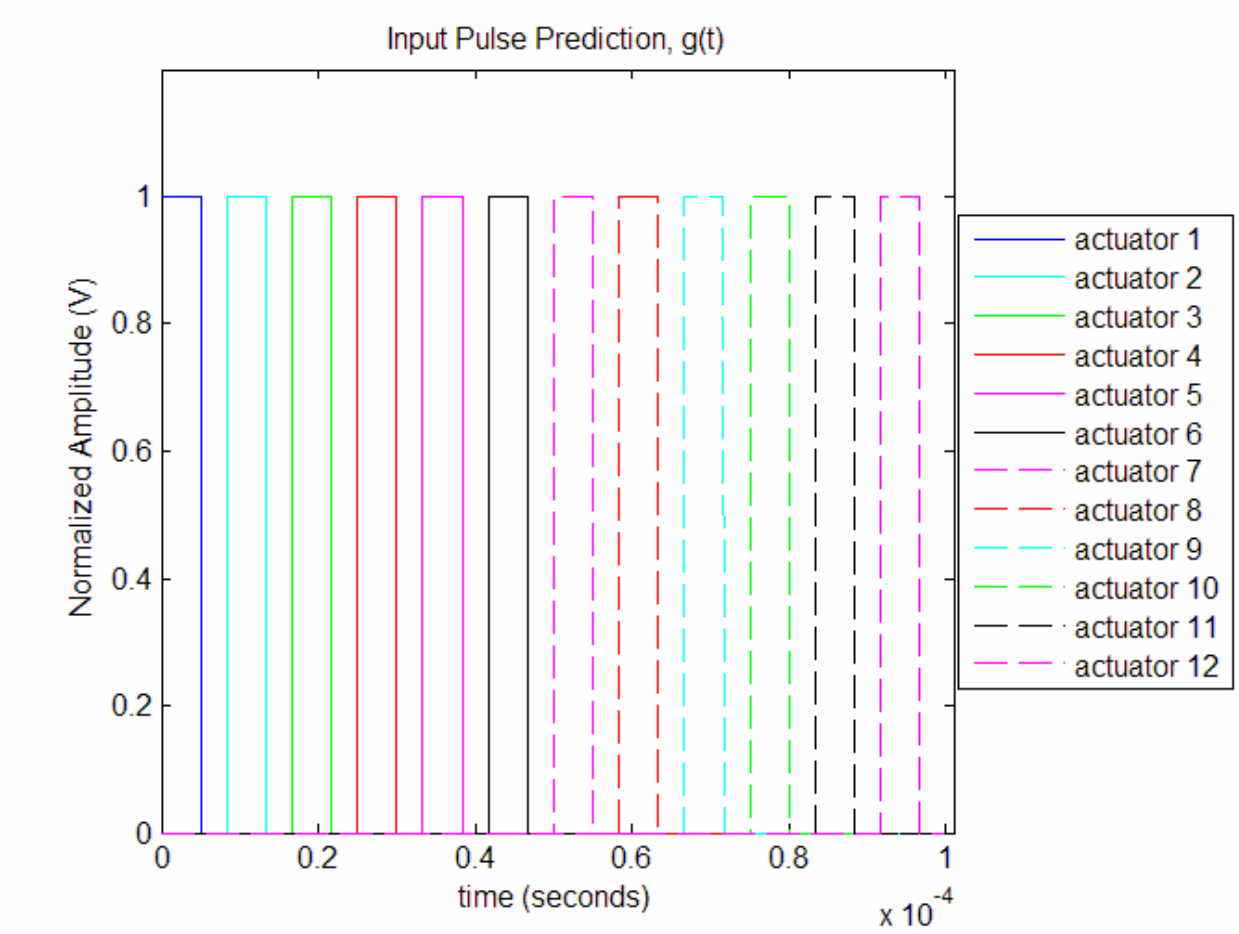

Figure 4.12: Input Pulse Simulation of Azimuthal Mode 1 for 10 kHz, 5% Duty Cycle

As previously described, the input pulses resemble rectangular waves. The input signal for all actuators was included in this plot. As seen in the plot, all actuators are turned on in a numerical sequence. Actuator 1 is fired first, followed by all other actuators in numerical order ending with actuator 12. Furthermore, in the case of azimuthal mode 1, all actuators are out of phase. However, this observation is not universal. As the azimuthal mode number changes, the individual input signals for each actuator continue to display the same rectangular shape, but the phase of each actuator changes according to the equations outlined in the previous section.

Beginning with azimuthal mode 2, not all actuators are out of phase. In fact, mode 2 defines that each actuator has a matching actuator in phase. For example, azimuthal mode 2 requires that actuators 1 and 7 have the equal phases and therefore identical operation. The same trend is observed for actuators 2 & 8, 3 & 9, 4 & 10, 5 & 11, and 6 & 12. Figure 4.13 demonstrates the simulated input signal for azimuthal mode 2 with a frequency of 10 kHz and a duty cycle of 10%.

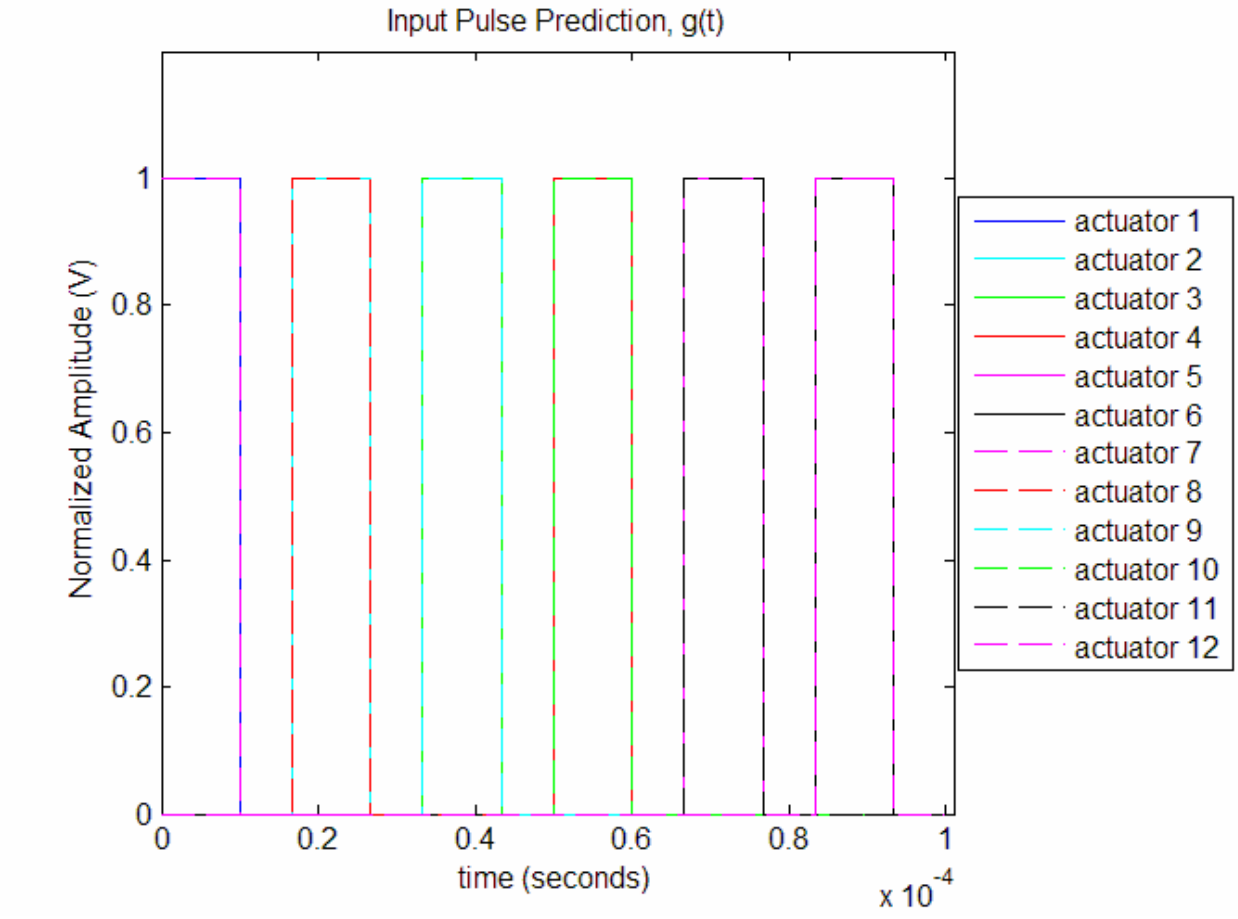

Figure 4.13: Input Pulse Simulation of Azimuthal Mode 2 for 10 kHz, 10% Duty Cycle

As seen in Figure 4.13, only 6 different phases occur in the input pulse signals for all actuators. As a result, each actuator has a corresponding mate that has the same actuation process during azimuthal mode 2. This same pattern is true for modes 3,

and 4. Mode 3 consists of four total phase changes, therefore requiring three actuators be in phase. Mode 4 reveals the same trend except four actuators are in phase, resulting in a total of three observed phases. Figures 4.14 and 4.15 demonstrate this principle.

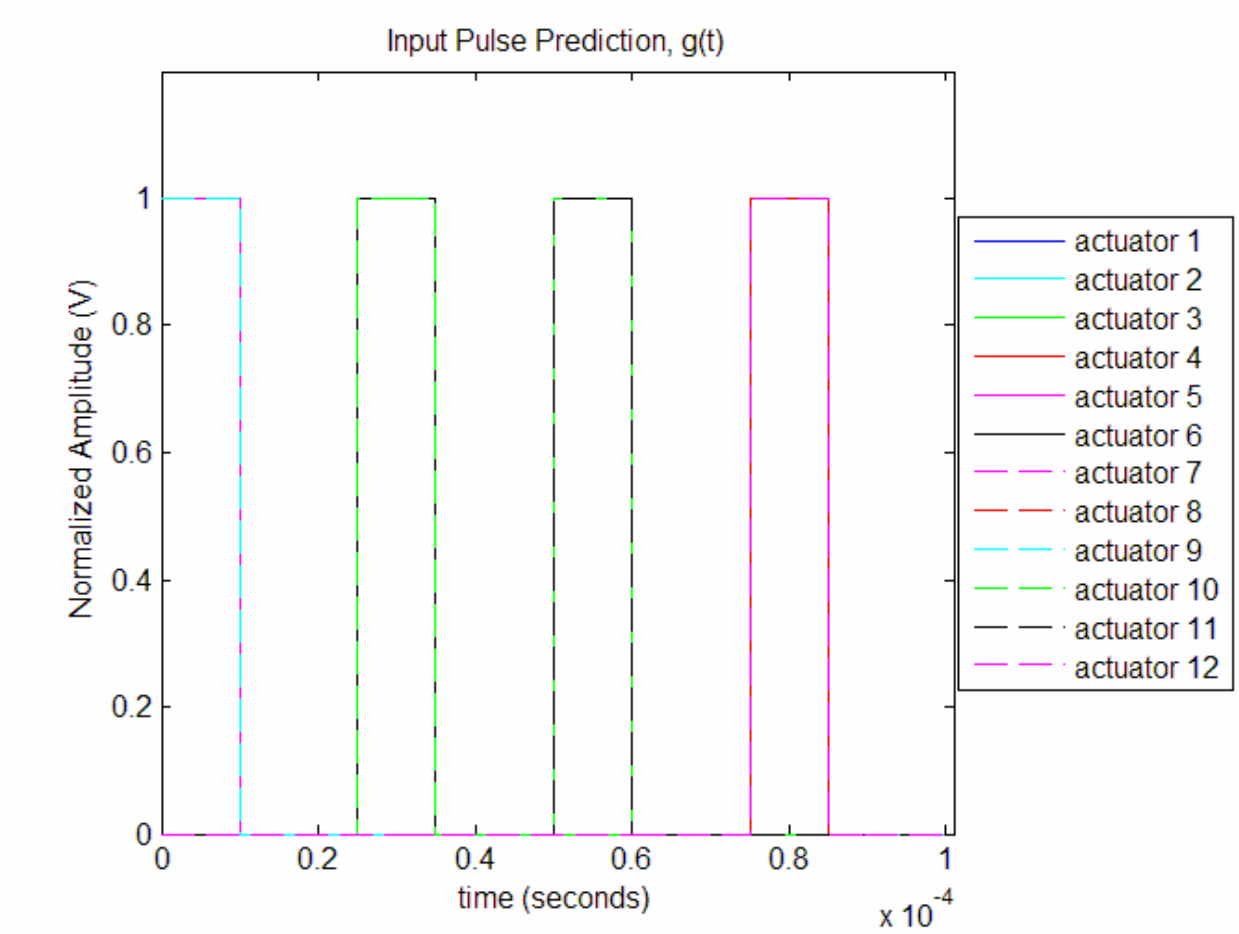

Figure 4.14: Input Pulse Simulation of Azimuthal Mode 3 for 10 kHz, 10% Duty Cycle

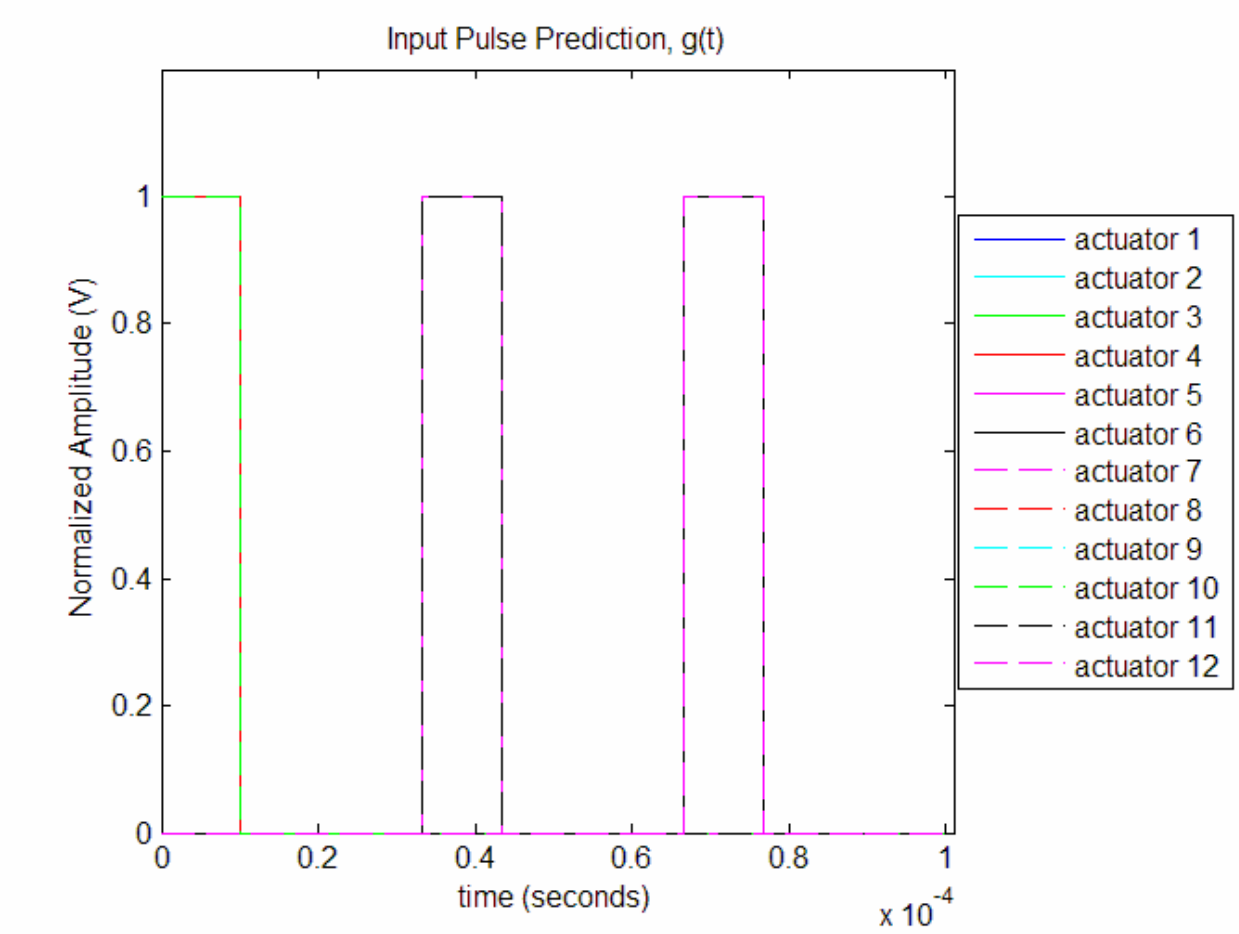

Figure 4.15: Input Pulse Simulation of Azimuthal Mode 4 for 10 kHz, 10% Duty Cycle

While modes 0, 1, 2, 3, and 4 provide easy understanding and solutions, azimuthal mode 5 presents various difficulties. Similar to mode 1, mode 5 does not allow any actuators to be in phase and twelve different input pulses are required for forcing. Figure 4.16 below depicts the input pulse function, *g(t)*, for azimuthal mode 5.

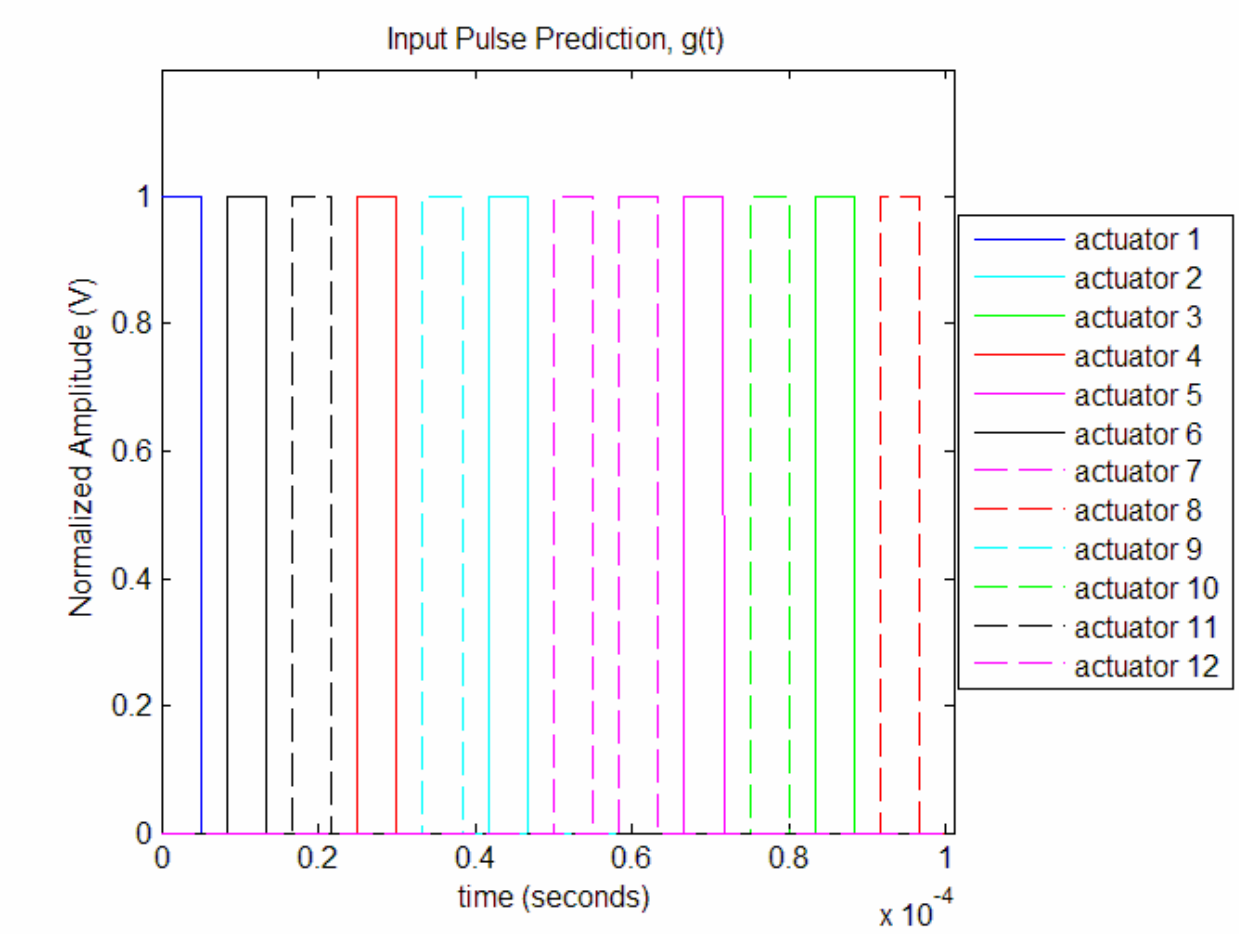

Figure 4.16: Input Pulse Simulation of Azimuthal Mode 5 for 10 kHz, 5% Duty Cycle

Similarly to the simulation for mode =1 in Figure 2, all of the actuators are out of phase. However, the same sequence for actuators is not observed. The time delay between actuators is much greater, resulting in a firing pattern that is not numerical.

Mixed modes add more complexity to the excitation of flow instabilities. While the mixed modes have many of the same underlying principles, these modes do not exactly follow the same patterns as the simple azimuthal modes previously discussed. All mixed modes consist of only two possible phases. The actuators "flap" back and forth between these two modes. These two phases are then used to mimic the combination of rectangular waves. When this combination occurs, nodes

and antinodes occur in the actuation sequence. Mode ±1 is created by considering the top half of the extension positive and the bottom half of the extension negative. Then, the actuations switch between positive and negative. After the first mixed mode, a pattern can be applied and the number of nodes in the mode is equal to twice the mode number. For example, mode = ±2 results in four nodes. Mode = ± 3 results in six nodes.

4.2.2. Actuator Output

As expressed in the previous section all actuators are in phase with azimuthal mode 0. Figure 4.17 demonstrates this mode through time discretized snapshots of an animation. This animation used a frequency of 10 kHz and 25% duty cycle. The four pictures represent 1 cycle, or 100 μs. The actuators are each represented by a pair of lines, or electrodes. In Figure 4.17, all green lines are ground wires while red lines are high-voltage wires. Furthermore, the blue portion shown in each snapshot represents the plasma arc that develops when the actuator is sent a positive voltage and turned on.

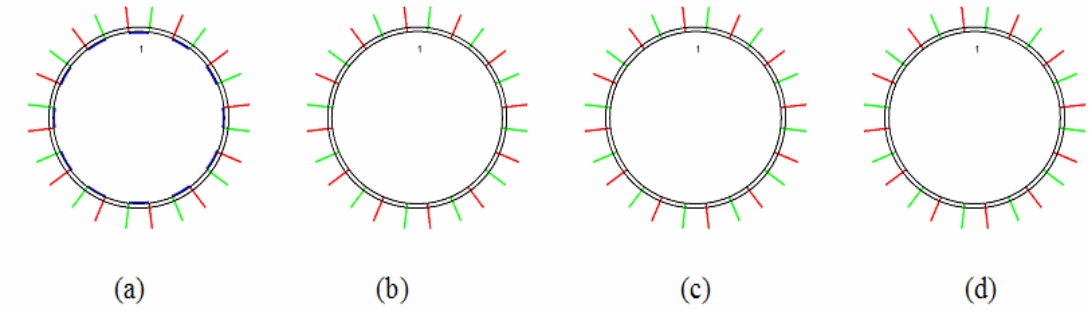

Figure 4.17: Actuator Animation for Azimuthal Mode 0 with f=10 kHz, duty cycle = 25%
(a) 0 μs (b) 25 μs (c) 50 μs (d) 75 μs

Due to the symmetry of the axisymmetric mode, all actuators are in phase and turn on with a time delay of 0 μs. In addition, after the time duration dictated by the pulse width, all actuators turn off for the reminder of the cycle. The on-time for all actuators corresponds to the duty cycle percentage of the total time period, 25 μs.

Figure 4.18 shows the same time-discretized snapshots of an animation of azimuthal mode 1. This animation used a frequency of 10 kHz and 8.33% duty cycle. All actuators are observed to turn on out of phase. In addition, all actuators turn on exactly once during one cycle and fire in numerical order.

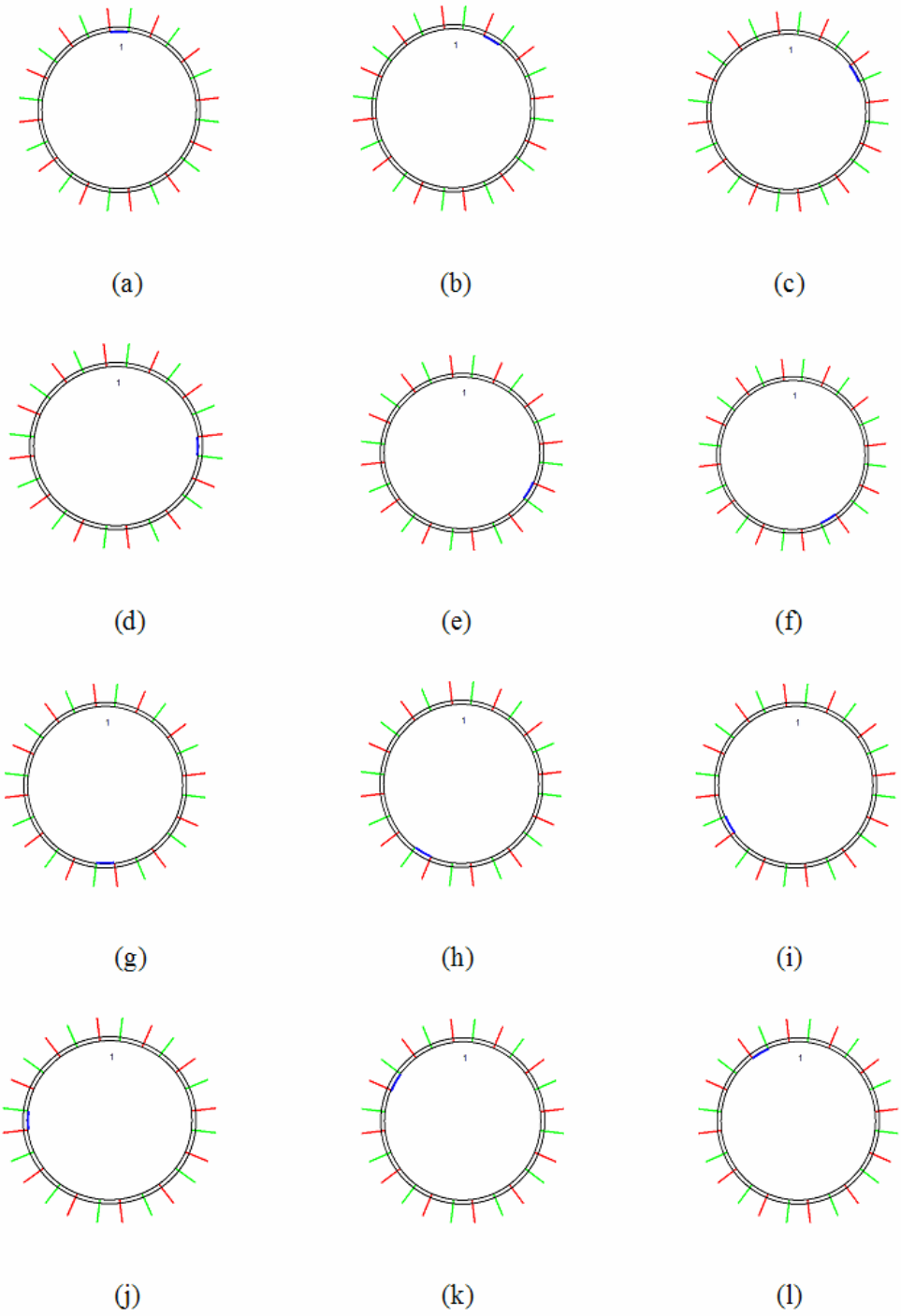

Figure 4.18: Time Discretized Schematic of Mode 1 for 8.33% duty cycle, f = 10 kHz
(a) 0 µs (b) 8.33 µs (c) 16.66 µs (d) 24.99 µs (e) 33.32 µs (f) 41.65 µs (g) 49.98 µs (h) 58.31 µs (i) 66.64 µs (j) 74.97 µs (k) 83.3 µs (l) 91.63 µs

Beginning with azimuthal mode 2, not all actuators are out of phase. In fact, mode 2 defines that each actuator has a matching actuator in phase. For example, azimuthal mode 2 requires actuators 1 and 7 to have the same phase and therefore identical operation. The same trend is observed for actuators 2 & 8, 3 & 9, 4 & 10, 5 & 11, and 6 & 12. Figure 4.19 demonstrates the simulated actuator response to the input signal for azimuthal mode 2 with a frequency of 10 kHz and a duty cycle of 16.67%.

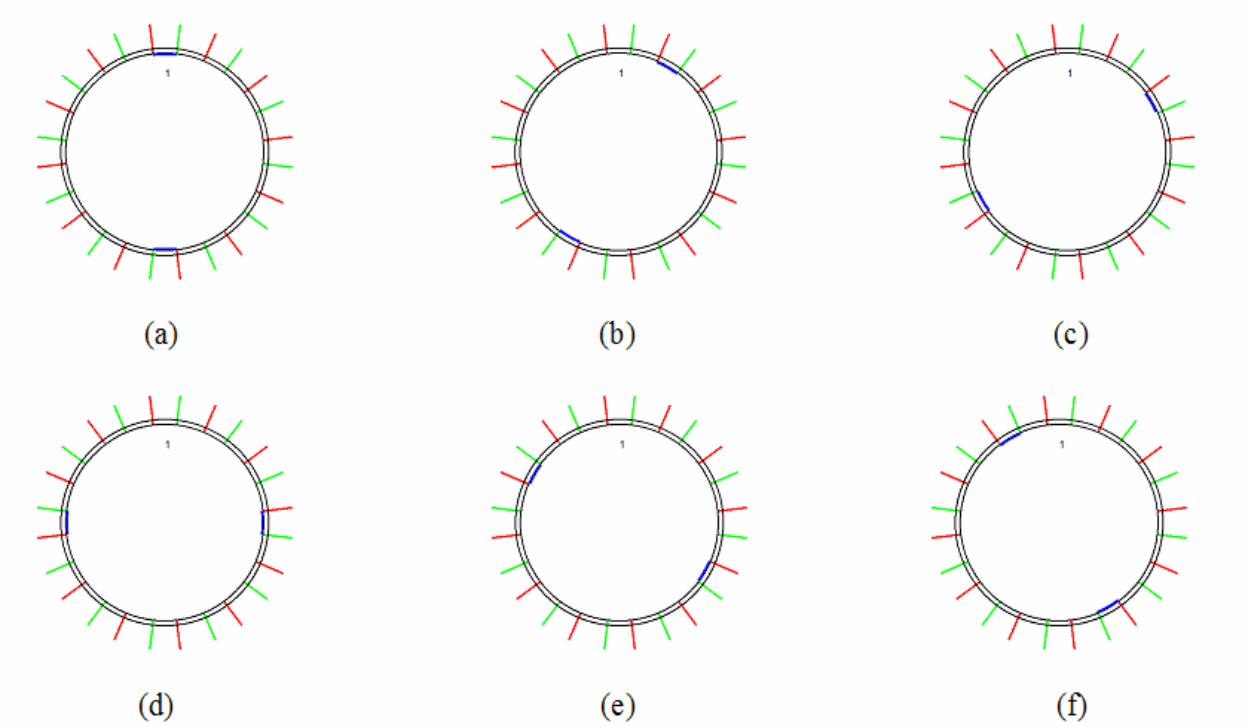

Figure 4.19: Time Discretized Schematic of Mode 2 for 16.67% duty cycle, f = 10 kHz
(a) 0 μs (b) 16.66 μs (c) 33.32 μs (d) 49.98 μs (e) 66.64 μs (f) 83.3 μs

As seen in Figure 4.19, only 6 different phases occur for all actuators. As a result, each actuator has a corresponding mate that has the same actuation process during azimuthal mode 2. This same pattern is true for modes 3, and 4. Mode 3 consists of

four total phase changes, therefore requiring that three actuators match up at a time. Mode 4 reveals the same trend except four actuators match up, resulting in a total of three observed phases. Figures 4.20 and 4.21 demonstrate this principle and all of these particular phases.

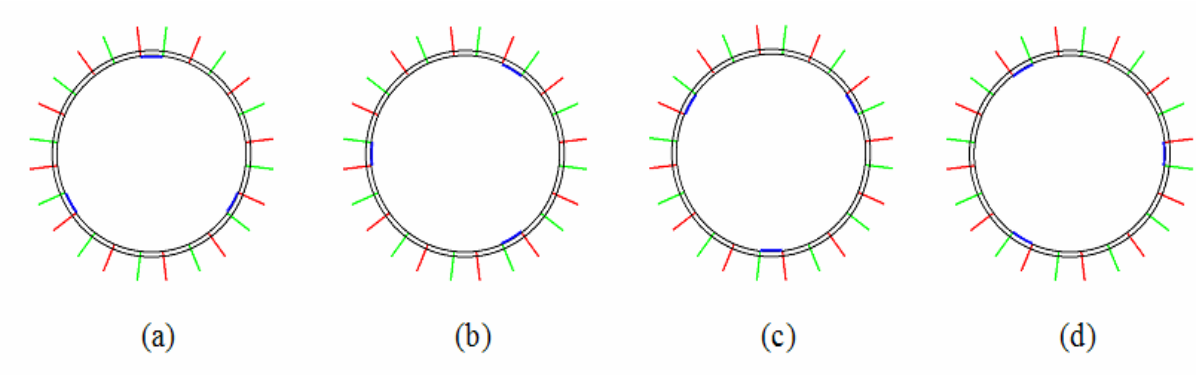

Figure 4.20: Time Discretized Schematic for Mode 3 for 25% duty cycle, f = 10 kHz
(a) 0 μs (b) 25 μs (c) 50 μs (d) 75 μs

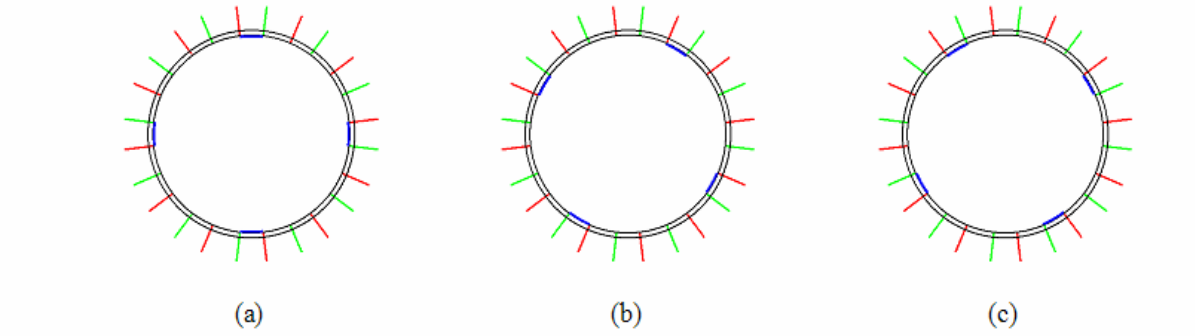

Figure 4.21: Time Discretized Schematic of Mode 3 for 33% duty cycle, f = 10 kHz
(a) 0 μs (b) 33 μs (c) 66 μs

In contrast to these azimuthal modes, mixed modes have different actuator responses. As previously described, the number of nodes corresponds to the mixed mode number, with ±1 as an exception. Figure 4.22 shows the node positions associated with mode with m = ±1. Additionally, the node positions associated with

mixed modes ±2, ±3, ±4, and ±6 can be seen in Figures 4.23, 4.24, 4.25, and 4.26 respectively.

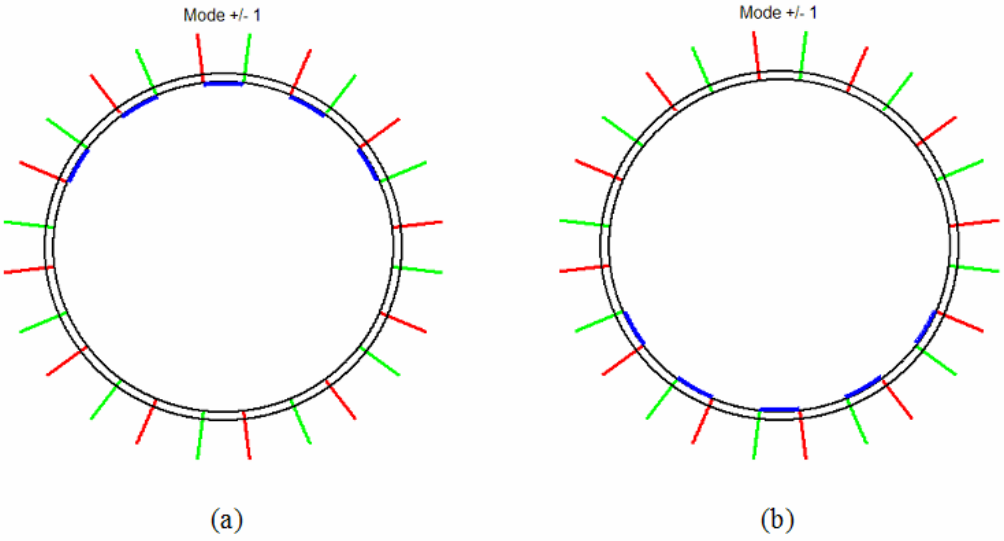

Figure 4.22: Actuator Nodes for Mixed Mode ±1

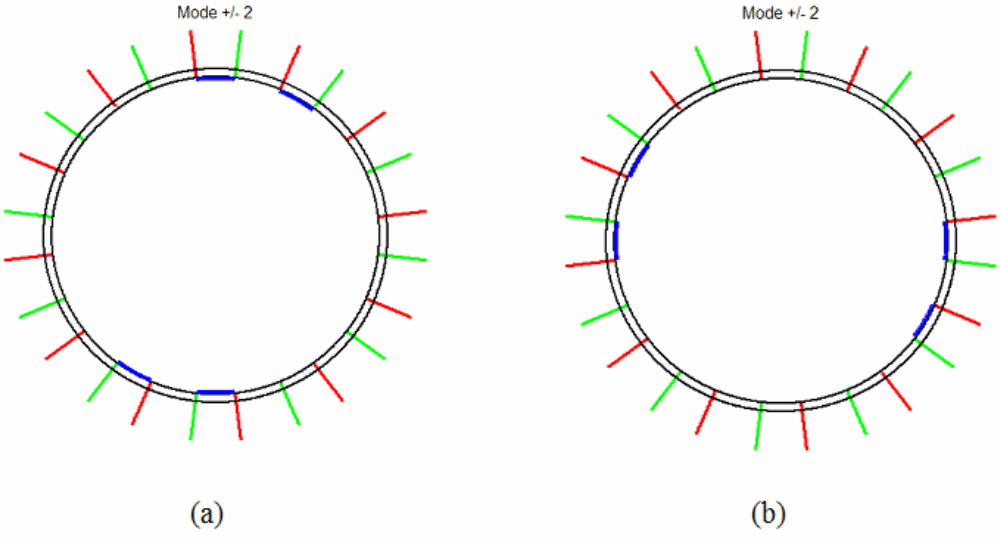

Figure 4.23: Actuator Nodes for Mixed Mode ±2

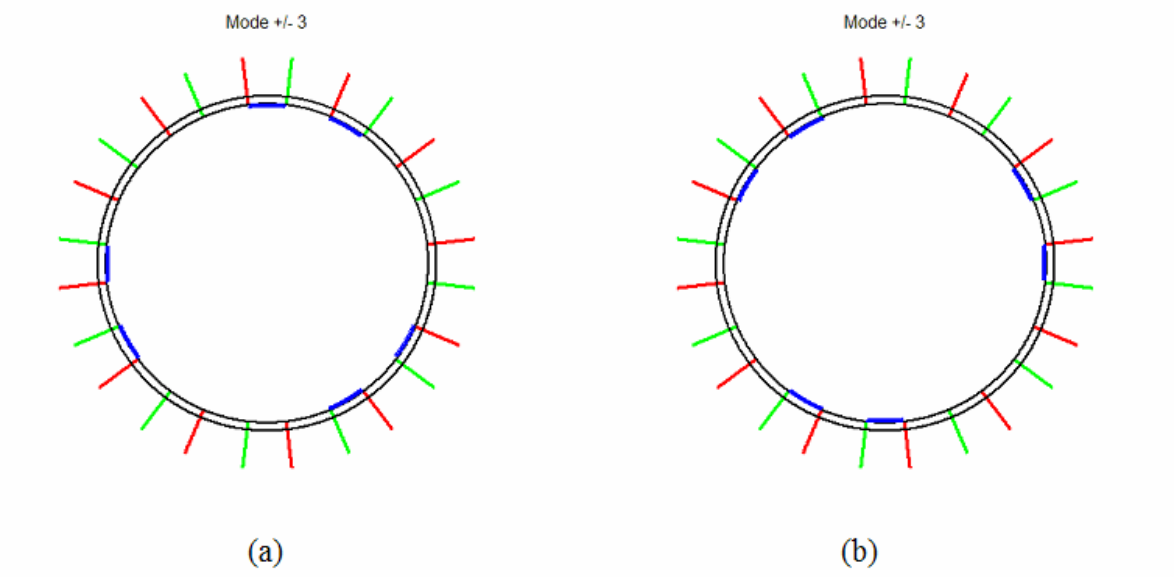

Figure 4.24: Actuator Nodes for Mixed Mode ±3

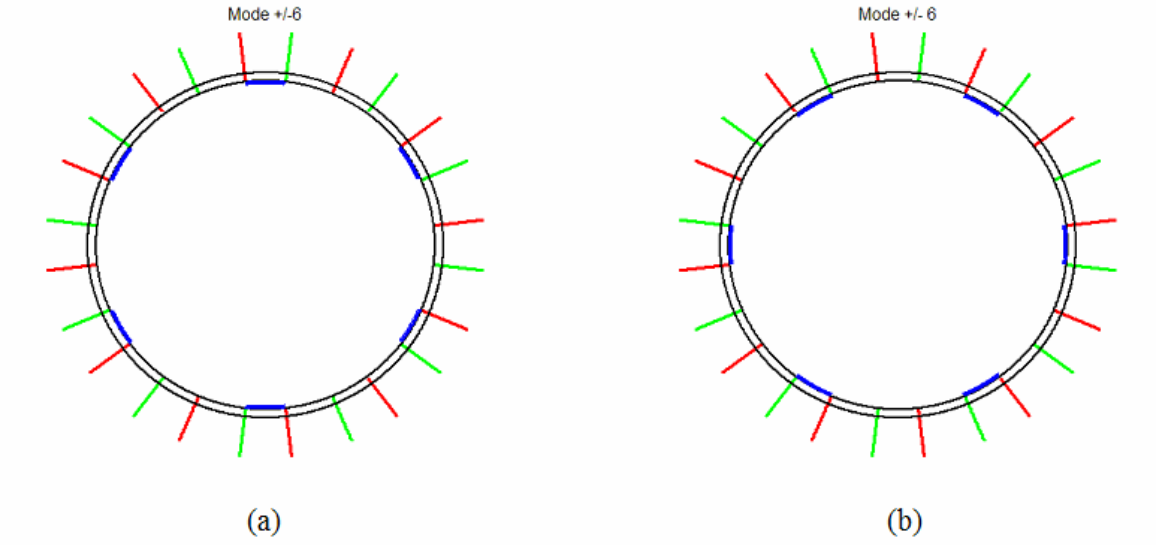

Figure 4.25: Actuator Nodes for Mixed Mode ±6

Only two phases were used to achieve all of the mixed modes. Therefore, the input pulse train for all mixed modes looked very similar. For all of the azimuthal modes

and mixed modes, the input pulse trains were created using a pulse generator. Details of this are included in the next section.

4.3. Control of Actuation

To force the flow at various azimuthal modes, the plasma actuators required individual operation during testing. To achieve this, multiple test setups were used. An 8-Channel digital-to-analog (DAC) PCI card and Labview software were used with modes that required eight phases or less. With this software, high-voltage outputs of approximately 10 kV, duty cycles from 0-100%, and forcing frequencies ranging from 0-200 kHz were obtained and utilized. This DAC and Labview software setup was the same for the eight actuator setup.

While this setup was sufficient for eight of fewer phases, it could not achieve azimuthal modes 1 or 5, which both require 12 different phases. To accommodate this need, two pulse generators were coupled. While capable of eight output signals, each generator was responsible for controlling six phases. Together, both generators operated the twelve phases required for azimuthal modes 1 and 5. Figure 4.26 below shows the pulse generators used for experimentation.

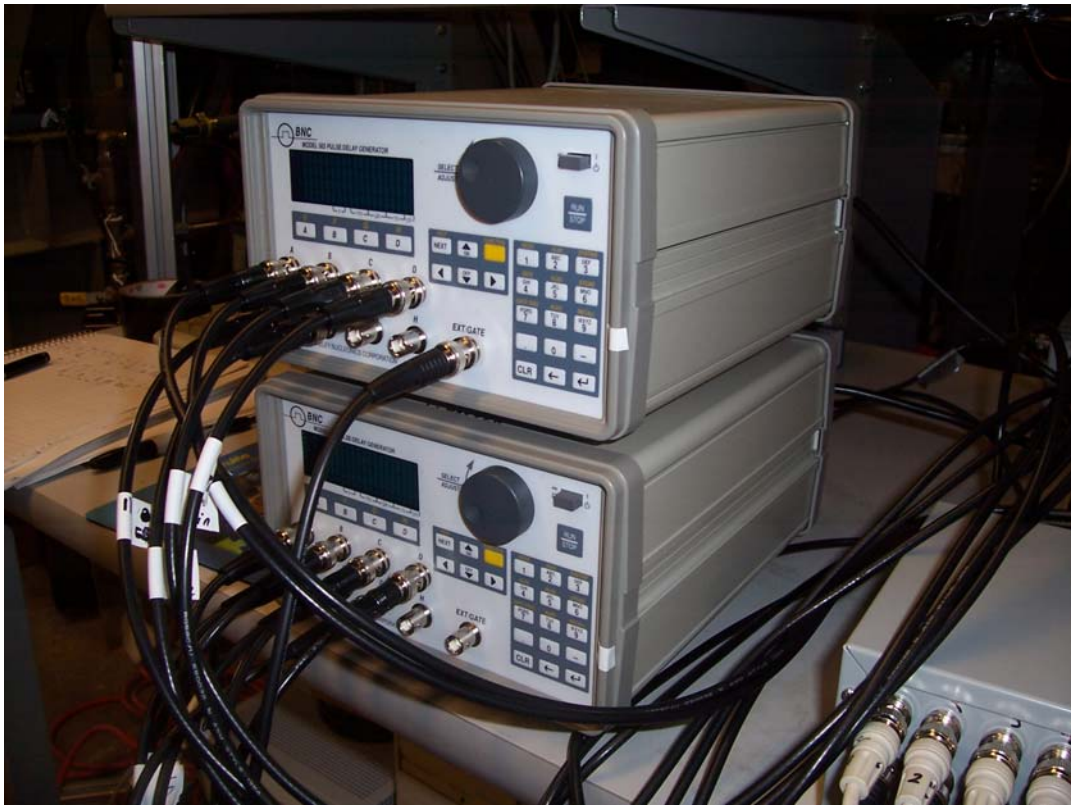

Figure 4.26: Pulse Generators Used for Experimentation

Both the pulse generator and DAC were used to create the input funtion *g(t)* for each test as previously discussed in Sections 2.3.2 and 4.2.1. After the appropriate input function is generated, the positive voltage of *g(t)* corresponds to the actuator turning on. The initial high voltage produced by this function across the positive and negative terminal of the actuator, breaks down the air in between. The breakdown arc is developed based on the atmospheric pressure. As soon as the air becomes appropriately ionized, the plasma arc develops and the voltage drops.

Figure 4.27 shows an example of the time-dependent input pulse train *g(t)*, voltage developed across the pin electrodes, current through the actuator, and power dissipated across the electrodes. For this example, four complete firings of the actuator were represented with a pulse width of approximately 15 μs.

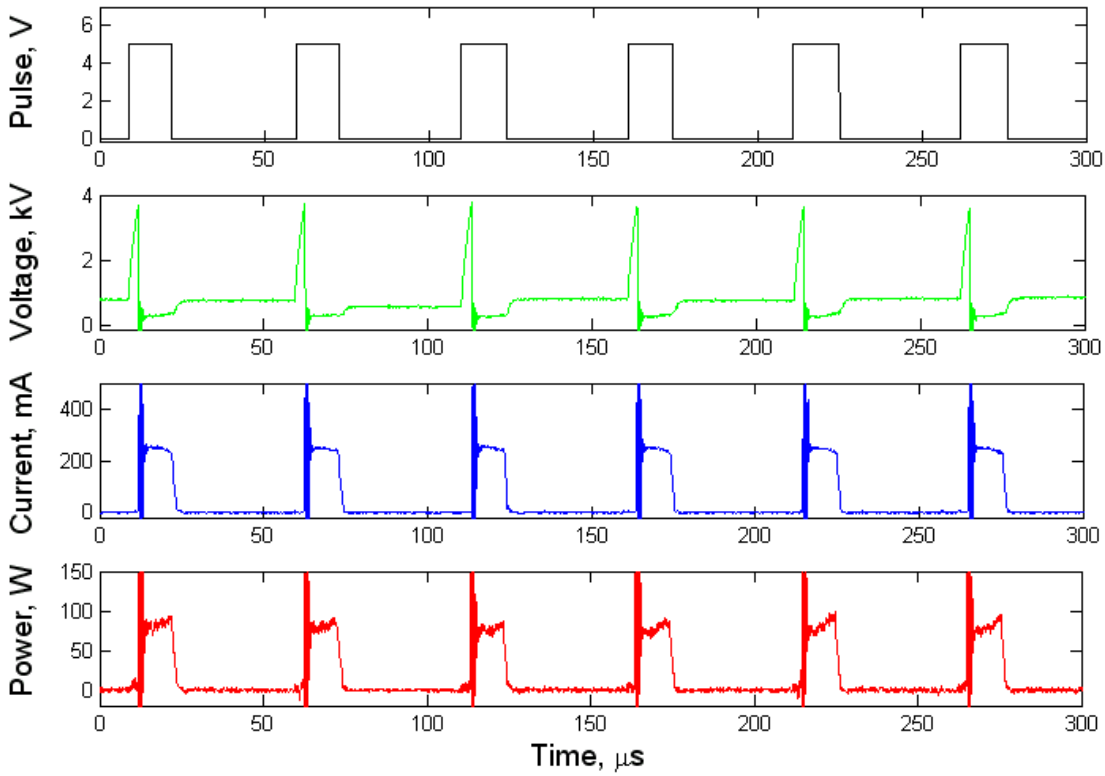

Figure 4.27: Time-Dependent Voltage, Current, and Power in a Plasma Actuator Operated at 20 kHz Frequency and 20% Duty Cycle

When the first trace, the input function *g(t)*, transitions from 0 V to approximately 5 V, the three other traces are generated in response. The second trace, the voltage developed across the pin electrodes, shows an initial spike to about 4 kV and then the signal levels off to approximately 500 V and remains steady. This spike corresponds to the breakdown arc previously discussed. The third trace, the current, also showed a spike at approximately 15 μs and then a flat section between 15 μs and 25 μs. The flat section of the current traces corresponds to the time duration of the plasma arc and the on-time of the actuator. The fourth trace, the power dissipated across the actuator, is the current trace multiplied by the voltage

trace. The maximum power dissipated displayed a trend that was similar to the current plot. The peak of the power was approximately 150 W per actuator, with a time-averaged power of approximately 30 W per cycle. This proved to very energy efficient, especially when compared to the power of the jet.

4.4. Experimental Setup and Facility

All experimentation was conducted at the Gas Dynamics and Turbulence Laboratory at The Ohio State University. Ambient air was dried, compressed, and stored in two cylindrical tanks with a volume of 36 m^3 at a pressure of 16 MPa. This air was then used for experimentation. The air was dried to ensure that no moisture was present during experimentation and therefore, avoid arcing in moist conditions.

The air was sent into a stagnation chamber where it was conditioned and then it was sent into an axisymmetric converging Mach 0.9 nozzle. The final portion of the stagnation chamber can be seen in Figure 4.28. This chamber was located just outside of the anechoic chamber.

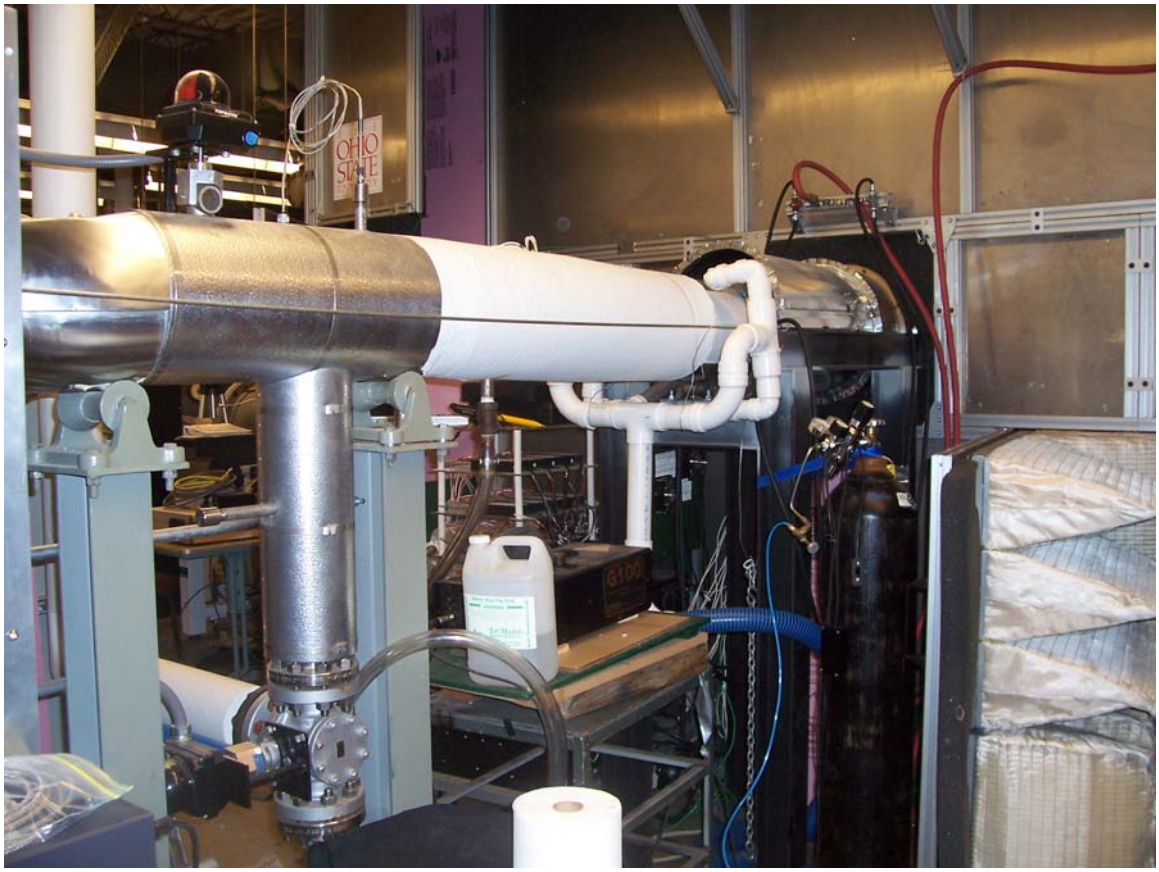

Figure 4.28: Portion of the Stagnation Chamber Directly Outside of the Anechoic Chamber

The exit diameter of the nozzle was measured to be 2.54 in. This nozzle was then connected to the adaptor and then the nozzle extension as previously discussed. Both the adaptor and nozzle extension were made of boron nitride and also had an inner diameter was 2.54 in order to provide a flush attachment. Twelve equally spaced actuators were mounted to the inside surface of the nozzle extension at the exit. The nozzle extension and actuators mounted in the flow facility can be seen in Figure 4.29. As seen in Figure 4.29, the actuators did not protrude into the flow to eliminate physical interference, allowing adiabatic heating to be the only source of actuation.

Figure 4.29: Nozzle Extension and 12 Actuators Mounted in Anechoic Chamber

The nozzle extension, adaptor, and actuators were mounted into the anechoic chamber at the Mach 0.9 nozzle. The flow was perturbed by the actuators and then it exited into the anechoic chamber. As side view of this setup can be seen in Figure 4.30.

Figure 4.30: Side View of Nozzle and Actuators in Anechoic Chamber

Two microphones were mounted inside the anechoic chamber to acquire acoustic measurements. These microphones were positions at 90° and 30° from the x-axis as seen in Figure 4.31. These positions were chosen based on the preference of certain noise components to propagate in particular directions. Shock noise and small scale structures are most likely to propagate at an angle of 90° and mixing noise and large-scale structures are most likely to propagate at an angle of 30°. Therefore, these two positions were monitored closely in order to determine the effects of plasma actuation on noise mitigation.

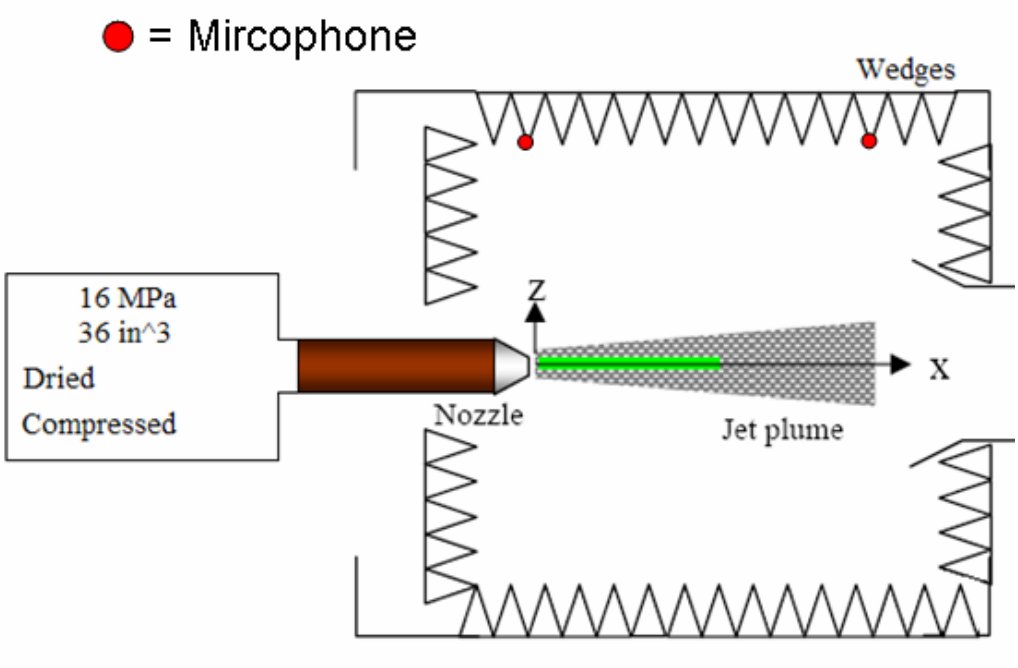

Figure 4.31: Schematic of the Experimental Flow Facility

4.5. Test Plan

Based on the experimental setup, it was desired to test the actuators at all of the possible azimuthal modes at various forcing frequencies. The available modes for 12 actuators were 0, 1, 2, 3, 4, and 5, with mixed modes ± 1, ± 2, ± 3, and ± 6. In addition, a range of forcing frequencies was determined based on previous research. The forcing frequency was described in terms of the non-dimension Strouhal number (St_D). The following equation outlines the forcing Strouhal number (St_{DF}), where f_F is the forcing frequency in Hz, D is the diameter in meters, and U is the jet velocity in m/s.

$$St_{DF} = \frac{f_F D}{U_j}$$

The frequency was varied based on test run while the diameter of the jet was help constant at 0.0254 m and the jet velocity was help constant at approximately 280 m/s.

Based on previous research, the jet is very receptive around the jet preferred mode. This mode, usually within a St_D range of 0.2-0.6, corresponded to a St_D of approximately 0.33 based on the current experimental facility. In accordance with this fact and the work completed with 8 actuators, the experimentation was performed with St_{DF}'s in the range of 0.1-5. This allowed for direct comparison between the 8-actuator setup and the new 12-actuator setup. Additionally, this gave a sufficient number of data sets to evaluate the effect of plasma actuation at higher aimuthal modes on noise mitigation.

The last parameter determined for the test plan was the duty cycle. Two approaches were considered when determining the duty cycle. The first involved a constant linear relationship between duty cycle and frequency as seen below in Figure 4.32. This method ensured that all actuations would occur in 10 μs pulses. During previous experimentation this duration was observed to be sufficient for arcing as well as cooling between runs.

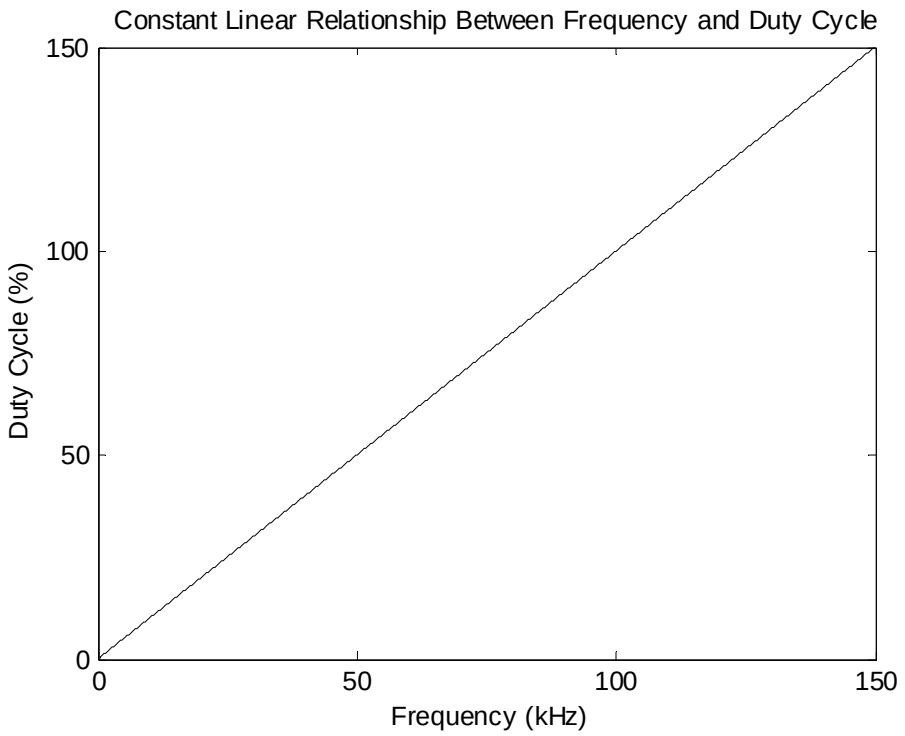

Figure 4.32: Constant Linear Relationship Method for Determining Duty Cycle

However, the constant duty cycle approach led to various restrictions in experimentation. It limited the maximum frequency to 100 kHz. At higher frequencies, the long pulse duration could prevent sufficient cooling between actuations. Therefore, another method was developed which allowed for a varying actuation time. This method, which was chosen for experimentation, can be seen below in Figure 4.33.

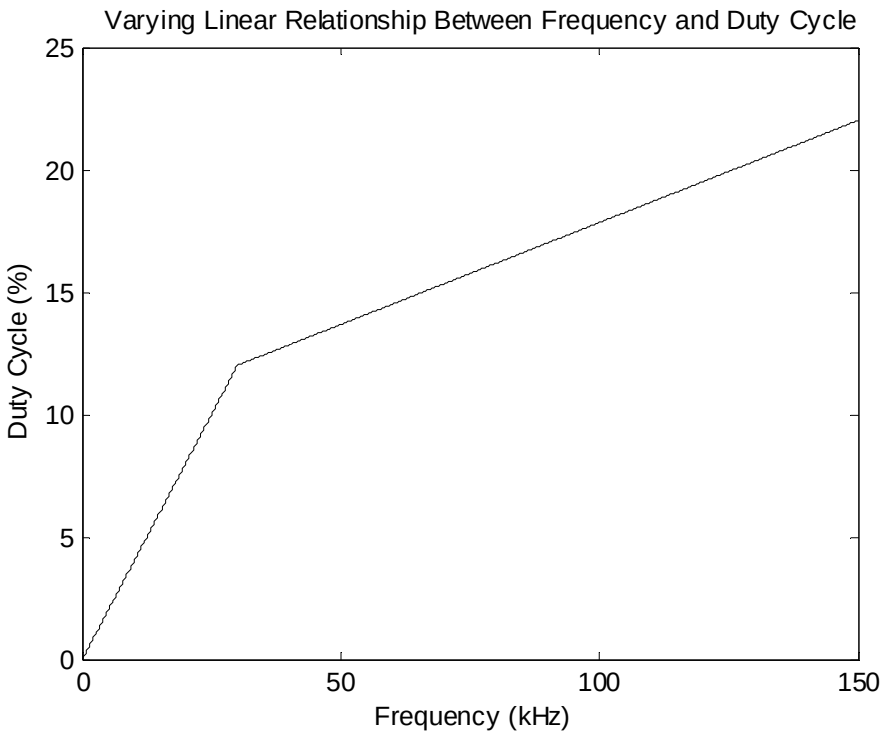

Figure 4.33: Varying Linear Relationship Method Used for Determining Duty Cycle

Based on the duty cycle, St_{DF} (forcing frequency), and azimuthal modes choices, testing was performed. The following section describes the steps taken to acquire and process sets of data.

4.6. Data Acquisition and Processing

Each test was conducted based on the equipment and test setup described in the previous sections. This testing consisted of exciting various azimuthal modes within the jet at appropriate St_{DF}'s and corresponding duty cycles. All of the sensors and setups previously described recorded the appropriate data sets during each run. The acoustic measurements were acquired at 30° and 90°. These measurements were

processed to evaluate the change in overall sound pressure level (OASPL) based on excited azimuthal mode. The details of this process were included below.

Sound Pressure Data Analysis

Sound pressure level values were recording using two ¼" B&K microphones. The microphones were mounted to the anechoic wedges at pressure angles of 30° and 90°, approximately 83D and 45D, or 85in and 45in away from the nozzle exit. During experimentation, the transducers were excited, producing an output voltage signal. This signal was amplified using a B&K Nexus conditioning amplifier and band pass filter from 20 Hz to 100 kHz. These microphones were calibrated in order to have a flat frequency response up to 80 kHz. The acoustic signal was obtained through the use of a *National Instruments* Labview DAQ board with a sampling frequency of 200 kHz. These pressure signals were used to evaluate the noise mitigation of the plasma actuation. The block diagram in Figure 4.34 demonstrates this flow of action.

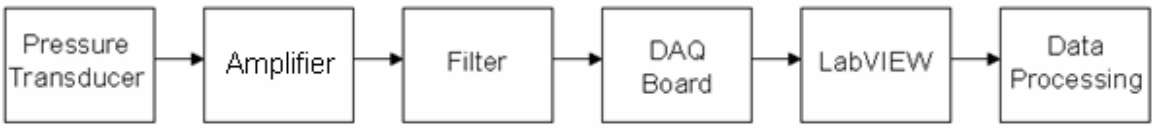

Figure 4.34: Block Diagram for Logic Flow

For a given St_{DF}, measurements were obtained at different azimuthal modes as well as the baseline case. These discrete pressure values were obtained and saved using MATLAB. Next, these very large data sets were analyzed using MATLAB script files. First, the data sets were divided into smaller, more manageable sets.

After this division, the time-domain pressure signals were converted to the frequency domain using an FFT. Large amplitude tones were observed at various times. Because they provided complications in data analysis, these tones were removed from the sound pressure using a technique similar to past researchers. For a particular forced case, the difference in amplitude between the baseline and the forced case was calculated at each discrete point. Using this pattern and level of amplitude, differences greater than 5 dB were capped, eliminating the tones and resulting in a smooth curve.

Given these results, an average sound pressure level was calculated for each particular St_{DF}. For all azimuthal modes and the baseline, these values were compiled into a St_{DF} (forcing frequency) vs. OASPL plot. Finally, the baseline sound pressure levels were subtracted from the average sound pressure level values to obtain the change in overall sound pressure level (ΔOASPL) based on the St_{DF} and azimuthal mode. These plots helped evaluate the effectiveness of plasma actuation on noise mitigation.

CHAPTER

5.0 RESULTS

As previously stated, all testing was performed in the Gas Dynamics and Turbulence Laboratory at The Ohio State University. After design of the components was completed, a test plan was developed. This test plan was carried out as previously described and acoustic measurements were taking. These data sets were processed as previously outlined. Details of the facility characteristic and processed acoustic data were included in the following subsections.

The results were divided into 2 categories: simple azimuthal mode and mixed azimuthal mode. The simple mode results included the OASPL measurements from forcing with m = 0, 1, 2, 3, 4, and 5. The mixed mode results included the same OASPL measurements for forcing with m = ± 1, ± 2, ± 3, and ± 6. With each set of measurements, the data from 12 actuators was compared to the previous data acquired using 8 actuators. Both differences and similarities were presented. The following sections include detailed discussion of the data sets.

5.1. Simple Azimuthal Mode Results

Figure 5.1 shows the acoustic results from actuation of azimuthal modes 0-5 at 90° and 30°. In general, the results from using 12 actuators are similar to the previous work using 8 actuators. Just as with 8 actuators, Figure 5.1 shows a maximum in the OASPL at a St_{DF} of approximately 0.33. This corresponded to the jet preferred mode, where the jet experienced the most spreading. The maximum OASPL level observed with 12 actuators was approximately 2.7 dB. This compared well to the maximum OASPL with 8 actuators of 2.5 dB as seen in Figure 5.2, reproduced from Figure 3.3. The minimal difference was attributed to both the extra energy being introduced into the system by the 12 actuators and the use of the more accurate pulse generator.

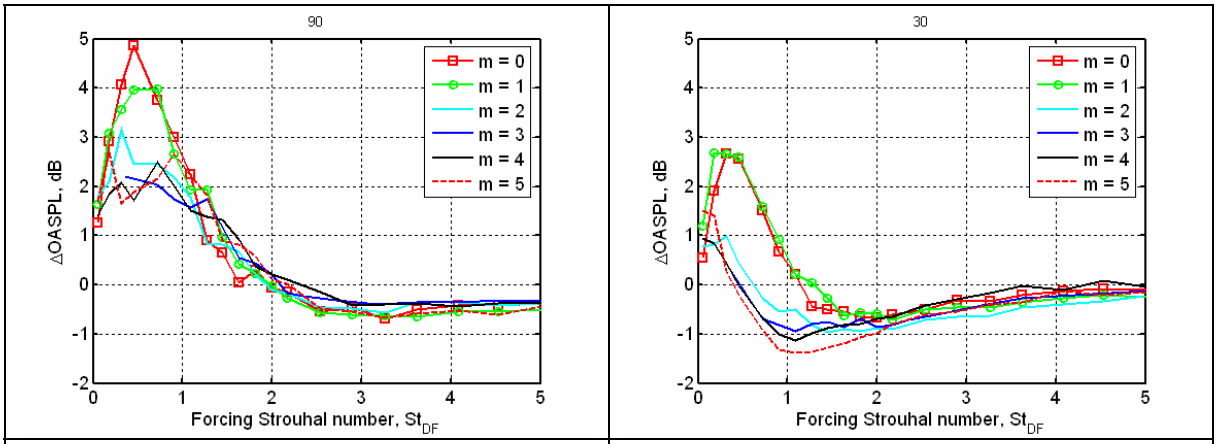

Figure 5.1: Change in OASPL for Azimuthal Modes using 12 Actuators

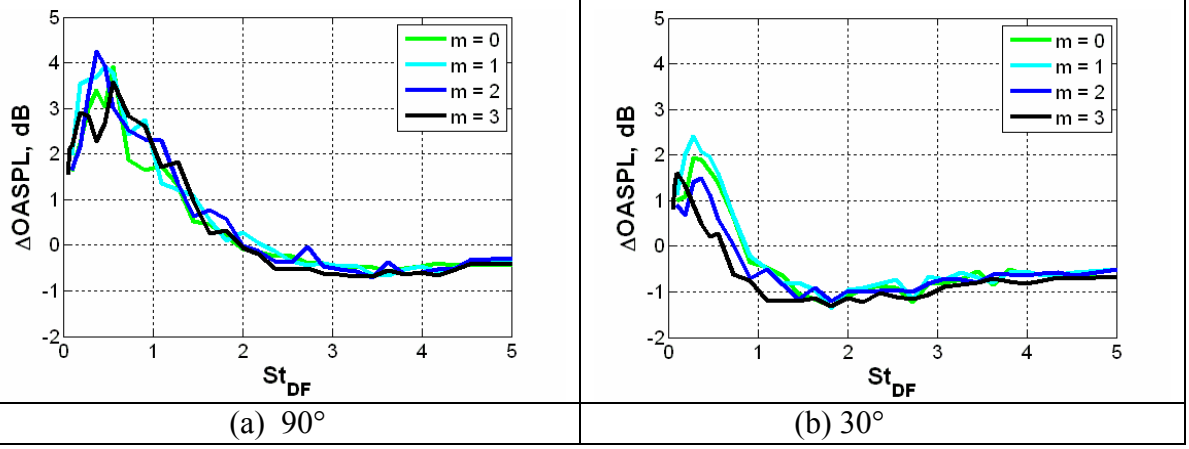

Figure 5.2: Change in OASPL for Azimuthal Modes using 8 Actuators (reproduced)

In addition to the peak at the jet preferred mode, the general shape of the results matched the results obtained with 8 actuators. As seen in both Figure 5.2 and Figure 5.1, the maximum OASPL at the jet preferred mode was followed by a significant decrease in the OASPL to a minimum around a St_{DF} of 1.3. This minimum was followed by a steady rise in OASPL with little observable difference between the azimuthal modes. This lack of difference showed that actuation above a St_D of approximately 2 does not affect the OASPL.

As predicted from the literature review and previous results, greater noise mitigation was observed at higher azimuthal modes, especially at mode 5. As seen in Figure 5.1(b), the OASPL dropped to approximately -1.3 dB at a Strouhal number of approximately 1. This showed an improvement in reduction of approximately 0.2 dB from the OASPL of -1.1 dB at azimuthal mode 3. Additionally, as seen in Figure 5.1 (a), the OASPL was kept under 2.9 dB.

However, a few differences were observed between the 8 actuator results and the 12 actuators results. With 8 actuators, the OASPL displayed a flat region between

Strouhal numbers of approximately 1 and 2.5, as seen in Figure 5.2 (b). In contrast, no flat region was observed with 12 actuators. Furthermore, as seen in Figure 5.1 (b), the OASPL quickly returns to 0 after reaching the minimum at a St_{DF} = 1.3. However, this same trend was not observed with previous work. Figure 5.3 (b) indicates that the OASPL increased very slowly after the minimum and only reached a value of approximately -0.6 dB. This difference in trend was attributed to the increase in energy addition associated with the increase in actuators.

5.2. Mixed Mode Results

In addition to the simple mode acoustic results, data sets were also obtained for mixed modes ± 1, ± 2, ± 3, and ± 6. Figure 5.3 shows the acoustic results for testing with the mixed mode actuation. In general, higher mixed modes led to a greater reduction in OASPL. Mixed mode ± 6 demonstrated very similar results to azimuthal mode 5 with a maximum noise mitigation at a St_{DF} of 1.3.

When comparing the mixed mode results to the azimuthal mode results, similarities and differences were discovered. Similar results were observed as the OASPL was amplified the most around a St_{DF} = 0.33. However, in comparison to the azimuthal modes, the ΔOASPL was larger for mixed modes. The peak OASPL at 30° was around 5 dB for ± 1 as compared to a maximum peak of 4.2 dB with m = 1. Just as with azimuthal modes, Figure 5.3 demonstrated that no differences in the OASPL occurred between various modes at St_{DF} greater than approximately 2 when the jet was excited with mixed modes.

Additionally, the results from the 12 actuator setup were also compared to previous experimentation with 8 actuators. The general shape of the results with 12 actuators was similar to that obtained with 8 actuators. This was observed by comparing Figures 5.3 and 5.4. However, at a St_{DF} greater than about 1.5, a difference was observed. With 12 actuators, the OASPL rose to a level close to 0 dB after reaching a minimum around St_{DF} = 1.3 as seen in Figure 5.3 (b). With 8 actuators, the OASPL increased to only 0.5 dB as seen in Figure 5.4 (b). Once again, this difference was attributed to the 50% increase in energy addition into the axisymmetric jet.

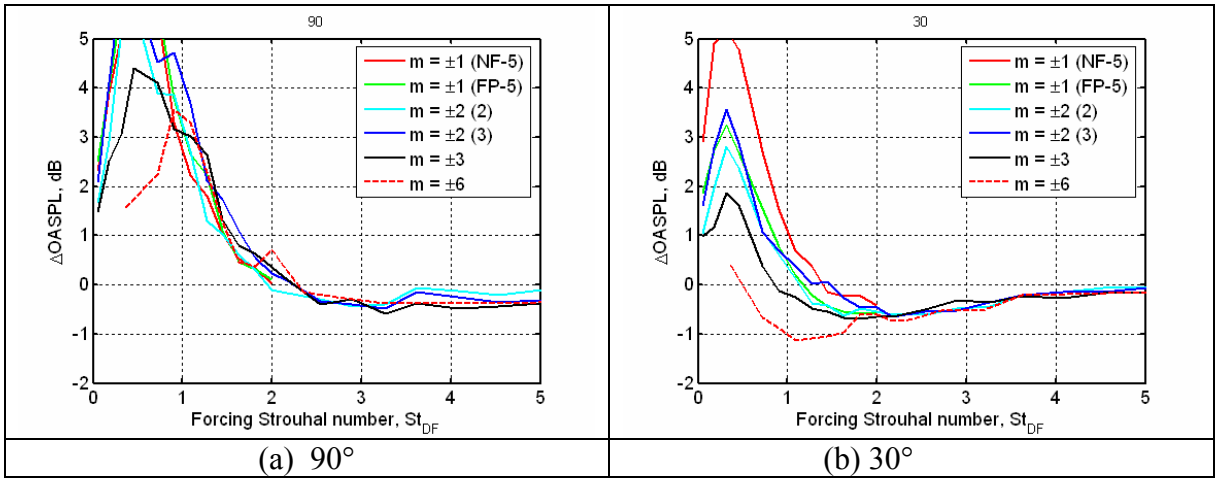

Figure 5.3: Change in OASPL for Mixed Modes at using 12 Actuators

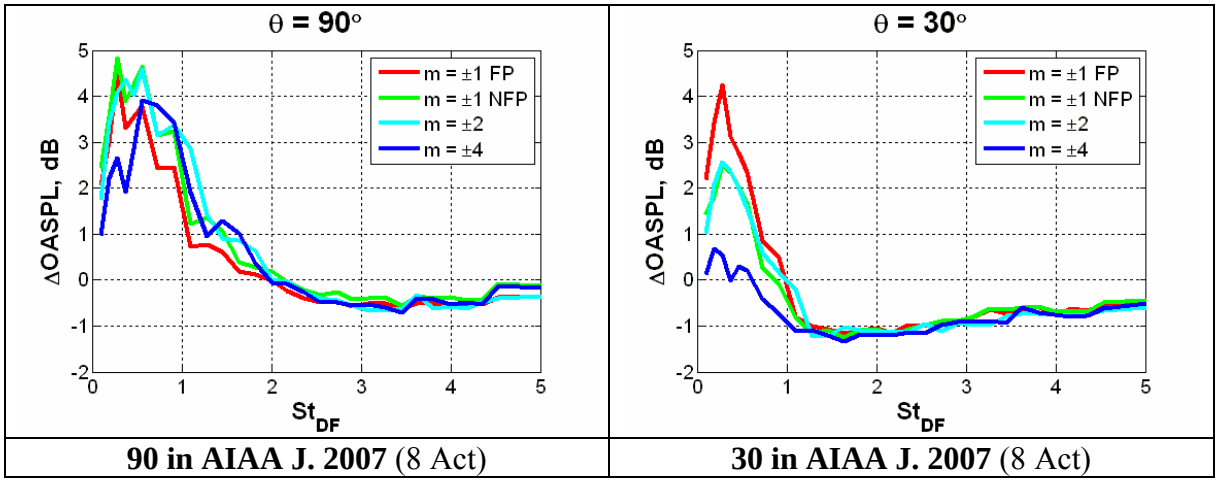

Figure 5.4: Change in OASPL for Mixed Modes using 8 Actuators (reproduced)

CHAPTER

6.0 CONCLUSION

Previous research at the Gas Dynamics and Turbulence Laboratory was performed using eight actuators distributed around the exit of a Mach 0.9 Nozzle. The axisymmetric jet was tested at various simple and mixed azimuthal modes. This testing revealed that the jet responded with mixing enhancement at the jet preferred mode and noise mitigation at higher modes. However, the eight actuator setup was restricted to a maximum simple mode of 3 and mixed mode of +/-4.

As a result, the eight actuator design was modified to house 12 actuators with the intention of reaching modes 5 and ± 6. With this modification, a new wiring system was defined with 12 channels. Additionally, an updated nozzle extension with 3 mm spacing was fabricated from boron nitride. In order to mount the new extension to the nozzle, an adaptor was designed and implemented.

With this new setup, simple azimuthal modes 0, 1, 2, 3, 4, and 5 and mixed azimuthal modes ± 1, ± 2, ± 3, and ± 6 were tested to observe the effects of plasma actuation on noise mitigation at higher modes. With all of the testing, maximum

mixing enhancement was seen at the jet preferred Strouhal number of 0.33. Additionally, higher azimuthal modes yielded greater noise mitigation. This was in line with the expectations of the project. Furthermore, the new results with 12 actuators were compared to the previous results with 8 actuators and both sets of results matched very well. This further supported the previous results and reinforced the validation of new results. Any subtle differences were attributed to the greater amount of energy being added to the system with the change from 8 actuators to 12. .

With any experimentation, there is always room for improvement. Further investigation Testing could be performed in order to see how the addition of plasma actuators changes the thrust of the jet. In addition, the characteristics of the jet could be changed in order to see if the plasma actuators are as effective. For example, heated jets could be used as opposed to those at ambient conditions.

- **REFERENCES**

[1] Little, J. "Development and Application of a Visualization Technique for Baseline and Controlled Cavity Flow." Undergraduate Thesis, 2004.

[2] Samimy, M., Kim, J.-H., Kastner, J., Adamovich, I., and Utkin, Y., "Active Control of High Speed and High Reynolds Number Jets Using Plasma Actuators," Journal of Fluid Mechanics, Vol. 578, pp. 305-330, May 2007.

[3] Samimy, M., J., Kim, Kastner, J.-H., Adamovich, I., and Utkin, Y., "Active Control of a Mach 0.9 Jet for Noise Mitigation Using Plasma Actuators," AIAA Journal, Vol. 45, No. 4, pp. 890-901, 2007.

[4] Utkin, Y., Keshav, S., Kim, J.-H., Kastner, J., Adamovich, I., and Samimy, M., "Use of Localized Arc Filament Plasma Actuators for High Speed Jet Control," Journal of Physics D: Applied Physics, Vol. 40, pp. 685-694, February 2007.